Innexin function dictates the spatial relationship between distal somatic cells in the *Caenorhabditis elegans* gonad without impacting the germline stem cell pool

Theadora Tolkin*[1], Ariz Mohammad*[2], Todd Starich[3], Ken C. Q. Nguyen[4], David H. Hall[4], Tim Schedl[#,2], E. Jane Albert Hubbard[#,1,5,6], David Greenstein[#, 3]

[1] Kimmel Center for Biology and Medicine at the Skirball Institute, NYU Grossman School of Medicine, New York, NY, United States

[2] Department of Genetics, Washington University School of Medicine, St. Louis, MO, United States

[3] Department of Genetics, Cell Biology and Development, University of Minnesota, Minneapolis, MN, United States

[4] Department of Neuroscience, Albert Einstein College of Medicine, Bronx, NY 10461

[5] Department of Cell Biology, NYU Grossman School of Medicine, New York, NY, United States

[6] Department of Pathology, NYU Grossman School of Medicine, New York, NY, United States

*****equal contribution

co-corresponding

23

24 **Abstract**

25

26 Gap-junctional signaling mediates myriad cellular interactions in metazoans. Yet, how gap
27 junctions control the positioning of cells in organs is not well understood. Innexins compose gap
28 junctions in invertebrates and affect organ architecture. Here, we investigate the roles of gap-
29 junctions in controlling distal somatic gonad architecture and its relationship to underlying
30 germline stem cells in *Caenorhabditis elegans*. We show that a reduction of soma–germline
31 gap-junctional activity causes displacement of distal sheath cells (Sh1) towards the distal end of
32 the gonad. We confirm, by live imaging, transmission electron microscopy, and antibody
33 staining, that bare regions—lacking somatic gonadal cell coverage of germ cells—are present
34 between the distal tip cell (DTC) and Sh1, and we show that an innexin fusion protein used in a
35 prior study encodes an antimorphic gap junction subunit that mispositions Sh1. We determine
36 that, contrary to the model put forth in the prior study based on this fusion protein, Sh1
37 mispositioning does not markedly alter the position of the borders of the stem cell pool nor of
38 the progenitor cell pool. Together, these results demonstrate that gap junctions can control the
39 position of Sh1, but that Sh1 position is neither relevant for GLP-1/Notch signaling nor for the
40 exit of germ cells from the stem cell pool.

41

42

43

44 **Introduction**

45

46 The relative positions of certain cells within larger organ structures are often important for
47 tissue function. Yet the mechanisms by which cells reach and maintain their precise relative
48 positions within organs are poorly defined. Gap junctions act as conduits for small molecules
49 passed between cells and/or as rivets to ensure adhesion between cells (reviewed by (Skerrett
50 and Williams, 2017)). They have also been implicated in cell morphology within organs
51 (reviewed by (Phelan, 2005)), however this latter role is less well characterized. Here we take

advantage of well-characterized and stereotypical morphology, interactions and relationships among cells in *Caenorhabditis elegans* to investigate the role gap junctions play in somatic gonad architecture and its consequences, or lack thereof, for the underlying germline stem cells.

The *C. elegans* hermaphrodite gonad provides a premier system for studying organogenesis and stem cell behavior (reviewed by (Hubbard and Greenstein, 2000; Hubbard and Schedl, 2019)). Two gonad arms, anterior or posterior of a central uterus and vulva, are each capped by a single somatic cell, the distal tip cell (DTC), that establishes a stem cell niche. Germline stem cells and their proliferative progeny, which together are referred to as progenitors, are maintained by GLP-1/Notch-mediated signaling in the germ line in response to DSL family ligands LAG-2 and APX-1 produced by the DTC (Austin and Kimble, 1987; Berry et al., 1997; Henderson et al., 1994; Nadarajan et al., 2009; Yochem and Greenwald, 1989). Proximal to the DTC, five pairs of sheath cells (named as pairs Sh1 to Sh5, distal to proximal) provide additional support to the germ line. In particular, Sh1 is implicated in promoting germline progenitor cell proliferation (Killian and Hubbard, 2005; McCarter et al., 1997). Although the molecular and cellular mechanisms by which Sh1 promotes germline proliferation remain to be fully elucidated, it is clear that one mechanism for the function of these cells involves the formation of gap junctions with germ cells (Starich et al., 2014).

Invertebrate gap junctions are formed from octameric hemichannels of innexin proteins (Oshima et al., 2016). In *C. elegans*, INX-8 and INX-9 associate to form hemichannels in the hermaphrodite somatic gonad which couple to germline innexin hemichannels (INX-14 with INX-21 or INX-22) to promote germline proliferation and inhibit meiotic maturation, respectively (Figure 1A–B; (Starich et al., 2014)). Phenotypic analysis of reduction-of-function mutants in *inx-8* recently led to the discovery of malonyl-CoA as a key cargo that traverses the soma-germline junctions to ensure proper embryogenesis (Starich et al., 2020) .

80 In the distal gonad, the somatic gonadal hemichannel components INX-8 and INX-9 are required
81 redundantly for germ cell proliferation and differentiation. Loss of both components renders
82 the germ line devoid of all but a handful of germ cells, which fail to undergo gametogenesis.
83 Restoration of *inx-8* either to the DTC or to Sh1 rescues the severe germline proliferation defect
84 of the *inx-8(0) inx-9(0)* double mutant. In addition, a reduction of *inx-8* and *inx-9* via
85 hypomorphic alleles or by RNA interference limits expansion of the pool of proliferative germ
86 cells (Dalfo et al., 2020; Starich and Greenstein, 2020; Starich et al., 2014).
87
88 Several observations point to a role for innexins in overall somatic gonad architecture. In young
89 adult hermaphrodites, the DTC forms long extending processes reaching proximally towards Sh1,
90 while the distal border of Sh1 is more regular, with filopodia extending distally towards the DTC.
91 Extensive ultrastructural and both fixed and live image analysis demonstrated the existence of
92 "bare regions" in between the proximal-extending DTC processes and the distal-extending
93 filopodial extensions of Sh1 in the adult hermaphrodite gonad. In these regions, germ cells are in
94 contact with neither the DTC nor Sh1, but are covered only by a basal lamina ((Hall et al., 1999);
95 Figure 1C and D). Interestingly, the hypomorphic allele *inx-14(ag17)* (Miyata et al., 2008) causes
96 Sh1 to reach almost to the distal end of the gonad (Starich et al., 2014) and to obliterate any bare
97 region between the DTC and Sh1. Similarly, a loss of bare regions was observed in *inx-8(0) inx-*
98 *9(0)* double mutants in which germline proliferation was largely restored through expression of
99 an *inx-8::gfp* transgene in the DTC only (Starich et al., 2014). This latter result suggested that if
100 Sh1 cannot form gap junctions with germ cells, Sh1 becomes distally mispositioned. However,
101 the consequences of this mispositioning and the accompanying loss of the bare regions for
102 germline stem cells has not been previously explored.
103
104 The spatial relationship between the DTC, Sh1 and the germ line summarized above was recently
105 challenged, and an hypothesis put forth that Sh1 might guide an oriented and asymmetric
106 division of stem cells, such that a daughter cell in contact with Sh1 enters the differentiation
107 pathway while the other, in contact with the DTC, remains a stem cell (Gordon et al., 2020). If
108 oriented cell fate-determining germ cell divisions occur in this way, the expectation would be

that germ cells undergoing such a division should be in contact with both the DTC and Sh1, and that closely spaced daughter germ cells that have recently undergone such a division would be remain in contact with one or the other. The model predicts that there should be few if any germ cells that contact neither the DTC nor Sh1. If Sh1 drives cell fate-determining germ cell divisions, another expectation would be that altering the position of Sh1 in the distal–proximal direction should similarly alter the position of the germline stem cell fate decision. However, given that much of the analysis was performed using an INX-8 fusion protein marker that could conceivably alter the position of Sh1, and given that the precise relationship between the position of Sh1 vis-à-vis the border of the stem cell pool was not investigated, we wished to determine how hypomorphic innexin alleles alter the position of Sh1 and whether the position of Sh1 influences the germline stem or progenitor pools.

In short, we characterize the natural variability of Sh1 position and confirm the presence of bare regions in gonads of early adult wild-type hermaphrodites. We show that reducing soma–germline gap-junction coupling causes Sh1 to be mispositioned distally. In addition, we show that the fusion protein used in the previous study (Gordon et al., 2020) encodes a dominant antimorphic allele of *inx-8* that also causes distal mispositioning of Sh1. Finally, we determine that when bare regions are absent due to Sh1 distal mispositioning, the borders of the stem or progenitor cell pools are not markedly altered. Together, these results demonstrate that while innexin function can dramatically impact the position of the distal border of Sh1, this position of Sh1 is not relevant for GLP-1/Notch signaling nor for germ cells to exit the stem cell pool.

Results

There is natural variability in the position of the distal border of Sh1, but gonads of wild-type hermaphrodites display bare regions where germ cells contact neither the DTC nor Sh1

136 We found that Sh1 is somewhat variably positioned in wild-type young adult hermaphrodites,
137 and we confirmed the existence of bare regions Sh1 and the DTC characterized by germ cells
138 that do not contact Sh1 or the DTC (Figure 1C–F; Video 1 and 2; Figure 1—figure supplement 1).
139
140 To better characterize the natural variability in the position of the distal border of Sh1 in the
141 wild type, and to facilitate comparisons among different genotypes and markers, we binned
142 gonads into one of three phenotypic classes based on the position of Sh1 (Figure 1C–F; Video
143 1–3; Figure 1—figure supplement 1). To avoid ambiguity that results from the analysis of
144 maximum projection images, we analyzed all gonads in 3 dimensions (based on 0.5 µm optical
145 Z-series slices). We designated as Class 1, those gonads in which >8 µm (a distance covered by 2
146 germ cell diameters) separated the DTC and Sh1. Class 2 includes those gonads in which Sh1
147 and DTC processes come within 8 µm or in which Sh1 extensions intercalate with DTC
148 processes, up to the position of the mean length of DTC processes. Class 3 gonads are those in
149 which the border of Sh1 is markedly shifted distally such that it lies between the distal end of
150 the gonad and the mean DTC process length.
151
152 Using *bcIs39[lim-7p::ced-1::GFP]* to visualize Sh1, a transgene that produces a CED-1::GFP
153 fusion protein that fully rescues the sheath cell function of CED-1 to engulf germ cell corpses
154 (Zhou et al., 2001), we found that a majority of gonads (70%) are in Class 1, confirming the
155 existence of bare regions. Indeed, in many cases the distance between the proximal-most DTC
156 measurement and the distal-most Sh1 measurement exceeds 25 µm (Figure 1G; Figure 1—
157 figure supplement 1 panel D). The remaining gonads are in Class 2.
158
159 Using three additional Sh1 markers (and one alternate DTC marker), we found that depending
160 on the markers used, 50–90% of gonads fall into Class 1, while Class 2 make up the remainder
161 (Figure 1—figure supplement 1). We note that both Class 1 and Class 2 gonads contain bare
162 regions with spacing of germ cell nuclei (as seen by differential interference contrast
163 microscopy) such that their surrounding cell boundaries are not plausibly in contact with the
164 DTC or Sh1. We did not observe Class 3 gonads in any wild-type worms examined.

165

166 We also analyzed serial distal-to-proximal transmission electron micrographs (TEM) of a gonad
167 from a wild-type unmarked young adult worm fixed using high-pressure freezing and freeze-
168 substitution freezing methods (Figure 1—figure supplement 2; Videos 4 and 5; Materials and
169 Methods). Focusing on an 80 µm region from the distal end to the distal extensions of Sh1, we
170 followed DTC processes (and their fragments) and Sh1 filopodial extensions among the tightly
171 packed germ cells (see Materials and Methods). We observed germ cells that contact neither a
172 DTC process (nor fragment thereof) nor filopodial extensions of Sh1, and thus represent bare
173 regions. Therefore, this TEM analysis is consistent with the confocal analysis above using cell
174 type-specific markers in live worms, and it corroborates prior ultrastructural observations made
175 on chemically fixed TEM preparations (Hall et al., 1999).

176

177

178 **Distal somatic gonad architecture is dictated by both somatic- and germline-expressed**
179 **innexins**

180

181 Previously, in fixed preparations, we observed that the distal edge of Sh1 was shifted nearly to
182 the distal end of the gonad in worms bearing a hypomorphic mutation in the germline innexin
183 *inx-14(ag17)* (Starich et al., 2014). We further investigated the position of Sh1 in *inx-14(ag17)*
184 using live imaging of intact young adult hermaphrodites bearing contrasting markers for Sh1
185 and the DTC (see Materials and Methods for details on markers used).

186

187 In contrast to *inx-14(+)*, the distal border of Sh1 in *inx-14(ag17)* extends to the distal end of the
188 gonad, well distal to the average position of the DTC processes (Figure 1C–E). The vast majority
189 of *inx-14(ag17)* gonads fall into Class 3 (Figure 1), with consistent results from three different
190 markers of Sh1 (Figure 1—figure supplement 1 panels B–E). Although our classification scheme
191 references Sh1 relative to DTC position, we do not attribute this gross positional alteration of
192 Sh1 to a change in the DTC. Instead, within strains with similar markers, the change in the *inx-*
193 *14* genotype does not significantly change average DTC mean process length or the length of

194 the longest DTC process, but it does have a significant effect on Sh1 distal border position
195 (Figure 1G; Figure 1—figure supplement 1 panel E).
196
197 Table 1 Brood sizes and embryonic lethality measurements for selected strains

Strain	Relevant Genotype[a]	Brood (n)[b]	%Lethality (n)[c]	Sh1 mispositioned [d]
N2	Wild type	298.6 ± 42.1 (24)	0.4 ±0.4 (7194)	no
DG5063	*inx-8(qy78)*[e]	221.6 ± 23.6 (25)	9.0 ±4.6 (6087)	yes
NK2571	*inx-8(qy78); cpIs122*	212.8 ± 27.5 (23)	6.2 ±3.0 (5217)	(yes[f])
DG5059	*inx-9(ok1502)*	322.7 ± 33.0 (25)	0.2 ±0.3 (8081)	(no[f])
DG5064	*inx-8(qy102) inx-9(ok1502)*[g]	211.1 ± 47.2 (25)	1.1 ±1.1 (5327)	(yes[f])
NK2576	*inx-8(qy102) inx-9(ok1502); cpIs122*	209.5 ± 52.7 (23)	2.3 ±1.2 (4928)	(yes[f])
DG5250	*inx-8(qy78tn2031)*[h]	260.0 ± 25.9 (25)	0.1 ±0.2 (6504)	(no[f])
DG5251	*inx-8(tn2034)*[h]	301.6 ± 37.8 (25)	0.4 ±0.4 (7570)	(no[f])
DG5270	*inx-14(ag17)*	253.2 ± 28.1 (25)	0.4 ±0.6 (6356)	(yes[f])
DG5070	*inx-14(ag17); inx-8(qy78)*	106.6 ± 19.4 (25)	23.7 ±8.0 (3510)	n.d.
DG5380	*bcIs39*	282.6 ± 34.2 (25)	0.4 ±0.5 (7091)	n.d.
DG5020	*naIs37; bcIs39*	237.5 ± 46.5 (24)	1.0 ±1.4 (5753)	no
DG5320	*fasn-1(av138::gfp) naIs37*	342.4 ± 30.3 (25)	0.4 ±0.4 (8591)	no
DG5367	*inx-14(ag17) fasn-1(av138::gfp) naIs37*	256.0 ± 26.6 (23)	0.2 ±0.2 (5897)	yes
DG5378	*fasn-1(av138::gfp) naIs37; inx-8(qy78)*	245.4 ± 43.7 (23)	5.3 ±3.2 (5947)	yes

215
216 [a]Full genotypes in Table S1; genotypes *inx-8(qy78[mKate2::inx-8])* and *inx-8(qy102[mKate2::inx-8])* are
217 abbreviated as "*inx-8(qy78)*" and "*inx-8(qy102)*" and *fasn-1(av138[fasn-1::GFP])* as *fasn-1(av138::gfp).*
218 [b]Brood size ± SD, n = number of broods counted
219 [c]Percent lethality ± SD, n = number of embryos scored
220 [d]yes/no indication of distal shift in the position of Sh1; relevant measurements in Figure 1, Figure 2, and
221 their related supplements.
222 [e]Derived from NK2571 *inx-8(qy78); cpIs122 [lag-2p::mNeonGreen::plcdeltaPH]* (Gordon et al., 2020).
223 [f]These particular strains were not scored for Sh1 position. However, where equivalent *inx* genotypes
224 were analyzed, the Sh1 phenotype is given in parenthesis; see Figure 1, Figure 2, and their related
225 supplements.
226 [g]Derived from NK2576 *inx-8(qy102) inx-9(ok1502); cpIs122* (Gordon et al., 2020).
227 [h]Equivalent *inx-8(null)* CRISPR-Cas9 deletions generated in *inx-8(qy78[mKate2::inx-8])* or in wild-type
228 genetic backgrounds.
229
230 To determine whether the position of Sh1 is shifted distally upon reduction of the somatic
231 innexins, we investigated the position of Sh1 relative to the distal end of the gonad in a well-
232 characterized compound reduction-of-function (rf) *inx-8* mutant ((Starich et al., 2020); Figure
233 1B–G). We found that Sh1 in worms bearing one partially functional somatic gonad innexin
234 encoded by *inx-8(tn1513tn1555)* in an otherwise null *inx-9(ok1502)* background (hereafter
235 referred to as "*inx-8(rf)*"; (Starich et al., 2020)) is also distally positioned, similar to *inx-14(ag17)*

236 (Figure 1C–E). Thus, Sh1 is positioned distally as a result of reducing the function of either germ
237 line or somatic innexins in the distal gonad.
238
239
240 **An mKate2::INX-8 fusion causes a distal shift in the border of Sh1**
241
242 We extended our analysis to *inx-8(qy78[mKate2::inx-8])*, an allele that encodes an N-terminal
243 fusion protein of mKate2 and INX-8 that was used to mark Sh1 in a prior study ((Gordon et al.,
244 2020); Figure 2A). As detailed below, we found that—like *inx-14(ag17)* and *inx-8(rf)—inx-*
245 *8(qy78[mKate2::inx-8])* caused a distal shift in the position of Sh1 (Figure 2B–F). We
246 documented this shift both by anti-INX-8 antibody (Starich et al., 2014) detection in otherwise
247 unmarked strains (Figure 2B–C), as well as in live imaging of marked strains (Figure 2D–F).
248
249 We used anti-INX-8 antibody staining to compare the distal border of Sh1 in the unmarked wild
250 type and in *inx-8(qy78[mKate2::inx-8])* gonads (N2 and DG5063, respectively; see Table S1;
251 Figure 2—figure supplement 1). The mean distal boundary of INX-8 staining in the wild type lies
252 at ~80 µm from the distal end of the gonad, while the mean distal boundary of INX-8 staining in
253 worms carrying *inx-8(qy78[mKate::inx-8)]* lies at ~50 µm from the distal end, and the difference
254 between these means is significant (Figure 2B–C). Moreover, in 89% of wild-type gonads (n=28),
255 the distal border of Sh1 is greater than 60 µm (~15-16 cell diameters) from the distal end of the
256 gonad, while in 79% of *inx-8(qy78[mKate2::inx-8])* gonads (n=32) the distal border of Sh1 is less
257 than 60 µm from the distal end (Figure 2B–C).
258
259 Similar results were obtained using live imaging. Using *bcIs39* to visualize Sh1, no Class 3 gonads
260 (n=27) are observed in the wild type, compared to 65% (n=26) in *inx-8(qy78[mKate2::inx-8)]*
261 (Figure 2D–E). We also observed that the same mKate2::INX-8 fusion in the background of the
262 *inx-9* null mutant (*inx-8(qy102[mKate2::inx-8])*, see Materials and Methods) also shifts Sh1
263 distally, while loss of *inx-9* alone does not significantly affect Sh1 position (Figure 2—figure

264 supplement 2). If mKate::INX-8 were innocuous, the *inx-8(qy102[mKate2::inx-8)]* allele in the
265 absence of *inx-9* (*inx-9(1502)*) should have had no effect on Sh1 position.
266
267 To explain the observed distal Sh1 border shift of mKate2::INX-8 compared to previous
268 descriptions of distal gonad architecture, Gordon et al. (2020) postulated that widely-used
269 markers of Sh1 driven by the *lim-7* promoter may not mark the entirety of the cell, excluding
270 the distal-most areas from detection. Although anti-INX-8 antibody staining clearly indicates a
271 more proximal position of Sh1 in otherwise unmarked wild-type strains and an evident distal
272 Sh1 shift in mKate2::INX-8, we wished to further determine whether the distal shift of Sh1 we
273 observed in *inx-8(qy78[mKate2::inx-8])* and *inx-14(ag17)* backgrounds reflected a disparity
274 between the expression patterns of mKate2::INX-8 and *lim-7p*-driven markers. First, we
275 consistently observe a dramatic distal shift of Sh1 in *inx-14(ag17)* using *lim-7* promoter-driven
276 transgenes (*bcIs39* and *tnIs5*) as well as using a functional endogenously tagged allele of the
277 fatty acid synthase gene *fasn-1*, [*fasn-1(av138[fasn-1::GFP])*] (Figure 1D; Figure 1—figure
278 supplement 1). We next examined the overlap between the mKate2::INX-8 and *lim-7p*-driven
279 markers in strains expressing both *inx-8(qy78[mKate2::inx-8])* and GFP markers encoded by
280 *tnIs6* [*lim-7p::gfp*] or *bcIs39* [*lim-7p::ced-1::gfp*]. In over 85% of gonad arms examined (n=20
281 and 26, respectively), the overlap between mKate2::INX-8 and GFP was complete (Figure 2—
282 figure supplement 3). In both *tnIs6* [*lim-7p::gfp*] or *bcIs39* [*lim-7p::ced-1::gfp*], the remaining
283 15% of gonads displayed either reduced Sh1 expression or expression in one but not both cells
284 of the Sh1 pair, which may result from stochastic transgene downregulation. Finally, we binned
285 these gonads into phenotypic Classes 1–3 based on measurements taken while observing either
286 mKate2 <u>*or*</u> GFP expression (Figure 2—Figure supplement 3 panel D). The number of Class 3
287 gonads is somewhat underestimated with the GFP markers. Nevertheless, we observe a marked
288 distal shift in the *inx-14* and *inx-8* mutants bearing these markers. In sum, if the GFP markers
289 were not marking the distal-most part of Sh1, we should not have been able to so readily detect
290 the abnormal distal displacement of Sh1 in *inx-14(ag17), inx-8(rf) or inx-8(qy78[mKate2::inx-8]*
291 strains bearing these markers.
292

293 We conclude that despite variability in the exact position of the Sh1 border, and despite minor
294 differences in transgene expression, bare regions between the Sh1 and the DTC are present in
295 the wild type, and they are greatly diminished due to a distal shift in the position of Sh1 in
296 worms bearing reduced *inx-14* or *inx-8* function or bearing the mKate2::INX-8 fusion.
297
298
299 **An mKate2::INX-8 fusion behaves as a dominant dosage-sensitive antimorph**
300
301 Based on our observations that *inx-8(qy78[mKate2::inx-8)])* gonads display a distally shifted
302 border of Sh1, we hypothesized that this allele might encode an INX-8 protein that poisons
303 innexin complexes thereby interfering with the channel and/or adhesion functions important
304 for Sh1 positioning. If this were due to a toxic effect of the mKate2::INX-8 fusion protein on gap
305 junctions, we would predict that the distal shift of Sh1 would be dependent on the presence of
306 the INX-8 coding region. To test this hypothesis, we used CRISPR-Cas9 genome editing to
307 generate *inx-8* null alleles in both the *inx-8(qy78[mKate2::inx-8])* and wild-type genetic
308 backgrounds. We generated deletions with identical breakpoints in the *inx-8* locus in both
309 genetic backgrounds [i.e., *inx-8(qy78tn2031)* and *inx-8(tn2034)*] starting 136 bp upstream of the
310 wild-type *inx-8* ATG start codon and extending 221 bp into *inx-8* exon 3 (Figure 2 and Figure 2—
311 figure supplement 2). In the *inx-8(qy78[mKate2::inx-8])* context, this deletion also removes the
312 mKate2 moiety. These deletions are expected to constitute *inx-8* null alleles because, in
313 addition to removing the start codon, they delete amino acids 1–349 (out of 382 amino acids),
314 including virtually all residues essential for spanning the plasma membrane and forming a
315 channel (Starich and Greenstein, 2020). Consistent with our hypothesis, the deletion mutant
316 *inx-8(qy78tn2031)* displays a significantly lower frequency of Class 3 gonads than the original
317 *inx-8(qy78[mKate2::inx-8])*. Sh1 in the deletion mutant is positioned more proximally, and
318 therefore, like the wild type, exhibits bare regions that are lacking in *inx-8(qy78[mKate2::inx-8])*
319 (Figure 2D–F). In addition, *inx-8(qy78tn2031)* exhibits a nearly normal brood size and
320 suppresses the low-level embryonic lethality observed in the *inx-8(qy78)* starting strain (Table
321 1). Likewise, the identical deletion generated in the wild-type genetic background, *inx-*

322 *8(tn2034)*, also exhibits the wild-type Sh1 position (Figure 2—figure supplement 2), with a
323 normal brood size and negligible embryonic lethality (Table 1). However, the observation of a
324 small percentage of Class 3 gonads in *inx-8(qy78tn2031)* and *inx-8(tn2034)* animals but not in
325 the wild type (Figure 2—figure supplement 2), suggests that the position of Sh1 is sensitive to
326 the dosage of somatic gap junction hemichannels. In fact, the *inx-8(qy78tn2031)/+*
327 heterozygote reveals apparent haploinsufficiency for this phenotype (Figure 2—figure
328 supplement 2).
329
330 We made several additional observations from a brood-size and embryonic-viability analysis
331 (Table 1). First, the marker transgenes do not have an appreciable effect on brood size or
332 embryonic lethality in our hands. Second, genetic interactions exist between *inx-*
333 *8(qy78[mKate2::inx-8], inx-14(ag17)* and the *inx-9(ok1502*) null mutation. Specifically, *inx-*
334 *14(ag17)* enhances both the reduced brood size and embryonic lethality of *inx-*
335 *8(qy78[mKate2::inx-8]*; whereas *inx-9(ok1502*) weakly suppresses the embryonic lethality
336 defect (Table 1). Third, in the course of this analysis, we noted that strains bearing *inx-*
337 *8(qy78[mKate2::inx-8]* displayed highly variable population growth dynamics that we attribute
338 to stress. Although the relevant stressor has yet to be determined, we observed this effect over
339 multiple generations after starvation or transport. Given our previous finding that key
340 metabolites such as malonyl-CoA are transported through these junctions to support
341 embryonic growth, this finding deserves future scrutiny.
342
343 Finally, to assess more fully the nature of the *inx-8(qy78[mKate2::inx-8]* allele with respect to
344 Sh1 position, we generated and imaged worms bearing this allele in heterozygous and
345 hemizygous configurations (Figure 2—figure supplement 2; we abbreviate *inx-*
346 *8(qy78[mKate2::inx-8]* to "*qy78*" and null to (0), below, to aid comparison between genotypes).
347 We infer loss-of-function behavior since other loss-of-function mutations affecting soma-
348 germline gap junctions, such as *inx-14(ag17),* also cause a distal shift in the Sh1 border.
349 Nevertheless, *inx-8(qy78)* is dominant: a substantial proportion of gonads in *qy78/+* are in Class
350 3, similar to *qy78/qy78,* but distinct from deletion heterozygotes [*inx-8(qy78tn2031/+*].

351 However, in a hemizygous configuration (*qy78/0*), the Sh1 distal displacement phenotype is
352 largely suppressed. Thus, *qy78* acts as a dosage-sensitive antimorph. We speculate that the
353 fusion protein produced by *inx-8(qy78[mKate2::inx-8])* can form dysfunctional junctions on its
354 own or with INX-8(+), but not when it is present below a certain abundance threshold. As also
355 mentioned above, the *inx-8* deletion allele *qy78tn2031*, while largely suppressing the Sh1 distal
356 mispositioning defect, displays a weak dominant haploinsufficient behavior consistent with
357 dosage sensitivity. Alternatively, this behavior could result from genetic positional effects that
358 impinge on nearby *inx-9* function and for which Sh1 position is particularly sensitive.
359
360 **The distal position of Sh1 does not influence the position of the stem cell pool border**
361
362 A recent model proposed that the position of the Sh1 border influences the stem/non-stem
363 decision in underlying germ cells (Gordon et al., 2020). However, because the previous study
364 did not examine the position of stem or progenitor cells, and because the model was based on
365 results using the antimorphic *inx-8(qy78[mKate2::inx-8])* allele, we investigated this
366 relationship.
367
368 In its simplest form, the model proposed by Gordon et al. (2020) predicts that when the distal
369 edge of Sh1 is positioned distally, the stem/non-stem border should similarly shift distally. The
370 SYGL-1 protein serves as a stem cell marker as *sygl-1* is a direct transcriptional target of GLP-
371 1/Notch in the germ line (Chen et al., 2020; Kershner et al., 2014; Lee et al., 2019; Lee et al.,
372 2016; Shin et al., 2017). We analyzed the proximal extent of the pool of SYGL-1-positive cells
373 bearing a well-characterized OLLAS epitope tag on SYGL-1 (Shin et al., 2017) and compared that
374 boundary relative to the distal Sh1 border (Figure 3 and Materials and Methods). In the case of
375 *inx-14(ag17),* though the distal border of Sh1 was shifted drastically and significantly, there was
376 no significant change in the position of the border of the SYGL-1-positive stem cell pool. In the
377 case of the *inx-8(qy78[mKate2::inx-8])* allele, the border of the SYGL-1-positive pool was
378 marginally shifted distally relative to the wild type, though not commensurate with the extent
379 to which Sh1 shifted distally in this background. Furthermore, the marginal shift of the border

380 of the stem cell pool in *inx-8(qy78[mKate2::inx-8])* was suppressed when *inx-8* was deleted in
381 both *inx-8(qy78tn2031)* and *inx-8(tn2034)*. The marginal shift in the border of the stem cell pool
382 is not observed in *inx-14(ag17),* suggesting that such a defect in *inx-8(qy78[mKate2::inx-8])* is
383 due to the altered function of mKate2::INX-8, rather than the position of Sh1 per se (Figure 3A-
384 C). To detect any subtle correlation between the proximal border of the SYGL-1 pool and the
385 distal border of Sh1, we plotted these against one another and computed an R value (Figure
386 3D). By Pearson correlation, there is no significant relationship in any genotype examined
387 between the position of the Sh1 border and the position of the SYGL-1-positive stem cell pool
388 border. There is no significant relationship regardless of whether measurements are made in
389 microns (Figure 3) or cell diameters (CD; Figure 3 and Figure 3—figure supplement 1).
390
391 The recent model also proposed that Sh1 controls spindle orientation at the stem/progenitor
392 border. However, we found that in the wild-type (marker-only) strain, the distal border of Sh1
393 was proximal to the proximal SYGL-1-positive border in 86% of the gonads (n=320), with a
394 distance between them of ≥5 CD in 67% of the gonads (Figure 3 and Figure 3—figure
395 supplement 1). As mentioned above, this 5 CD distance is inconsistent with the hypothesis that
396 Sh1 is controlling spindle orientation at the stem cell border as such control would be expected
397 to occur over a distance of only 1–2 cell diameters.
398
399 We conclude that (1) there is no correlation between the position of the distal border of Sh1
400 and the proximal border of the SYGL-1-positive stem cell pool, and (2) if spindle-oriented
401 divisions occur at the Sh1 border, they are not influencing stem cell fate.
402
403
404 **The distal position of Sh1 does not influence the position of the progenitor pool border**
405

406 Although we found no correlation between the stem cell pool border and Sh1 position, we
407 wondered whether altered Sh1 position might nevertheless influence the position of the border
408 between the progenitor zone (PZ) and the transition zone that marks overt meiotic entry. In the

409 wild type, consistent with our previous analysis in live worms, we found that the distal position
410 of Sh1 is somewhat variable and can be either distal or proximal of the PZ border, using the
411 length of the CYE-1-positive region to define the PZ border, following CYE-1 and pSUN-1(S8) co-
412 staining (Figure 4 and Materials and Methods; Mohammad et al., 2018). We found that
413 although there is a subtle shift in the PZ border in *inx-8(qy78[mKate2::inx-8])* and *inx-14(ag17)*,
414 it does not correlate with the dramatic shift in Sh1 position seen in these mutants (Figure 4).
415 Again, we saw no significant correlation between Sh1 position and the position of the PZ border
416 (Figure 4D). As with the SYGL-1 analysis, the relationships are similar when measurements are
417 made in microns (Figure 4) or in CD (Figure 4—figure supplement 1), noting that differences
418 between genotypes are more apparent in the micron measurements since cells are slightly
419 larger more proximally in the PZ.

420 In sum, the border between the PZ and the transition zone is not markedly altered relative to
421 the dramatic distal displacement of the Sh1 border in *inx-14(ag17)* or in *inx-*
422 *8(qy78[mKate2::inx-8]*, suggesting that the position of Sh1 has no bearing on the position of
423 meiotic entry.

424

425

426 **Discussion**

427

428 These studies show that impaired innexin function distally mispositions Sh1, but that this
429 displacement does not similarly shift the proximal border of the stem cell pool (Figure 5). We
430 show that bare regions of variable size normally exist between the DTC and Sh1, in which germ
431 cells lack contact with the DTC or Sh1, but that these bare regions are diminished or lost with
432 reduced innexin activity either in the soma or the germ line. These findings offer a unified
433 explanation for a previous observation of loss of bare regions between the DTC and Sh1 in
434 strains carrying an mKate2::INX-8 fusion marker that, we now determine, is interfering with
435 innexin function. We concur with the previous observation: bare regions are lost in strains

436 carrying this fusion. The previous interpretation was that the mKate2::INX-8 was marking a
437 distal-most part of Sh1 that was not detectable with other markers. This led to a model
438 whereby Sh1 influences the stem cell fate decision in the underlying germ cells. Instead, we
439 show that the mKate2::INX-8 fusion itself alters innexin function such that Sh1 is distally
440 mispositioned and this mispositioning obliterates the bare regions. Our interpretation is
441 consistent with results obtained by TEM analysis (Hall et al., 1999; this work), antibody staining
442 (Starich et al., 2014; this work), and live imaging in strains bearing different fluorescent proteins
443 expressed in Sh1, as well as our genetic analysis. The cautionary tale is that fusion proteins used
444 as markers, even when they are generated by CRISPR/Cas9 genome editing in the context of
445 the endogenous locus—and therefore are not likely mis-expressed or overexpressed—may
446 nevertheless generate proteins that are not benign. Here, the mKate2::INX-8 fusion protein
447 caused a distal shift in the Sh1 position due to its apparent antimorphic effect on gap junctions.
448 Because of the redundant function of INX-9, we were able to remove the mKate2::INX-8 protein
449 entirely and effectively restore the bare region.
450
451 Our finding that the germline response to signaling from the DTC, as measured by expression of
452 the GLP-1/Notch target, SYGL-1, is independent of germline interactions with distal sheath cells
453 (Sh1) is consistent with several other observations. For example, males, which lack sheath cells
454 altogether, exhibit stem cell pools similar to those in the hermaphrodite (Crittenden et al.,
455 2019). In addition, the stem cell and progenitor pools are present in larval stages prior DTC
456 process elaboration (Byrd et al., 2014), when Sh1 is positioned several CD from the DTC,
457 precluding the possibility of a DTC–Sh1 handoff at these stages (Killian and Hubbard 2005).
458 Here, we observed that the distal border of Sh1 relative to the proximal stem cell border in the
459 wild type is ≥5 CD in the majority of gonads we examined. Thus, the previous model that Sh1
460 orients divisions of stem cells to direct their fate is also called into question by our results.
461 Finally, using alleles that dramatically alter the position of Sh1, we found no evidence
462 supporting the prediction that the stem/non-stem border is coincident with the Sh1 border.
463 Together, these results indicate that Sh1 is not involved in the germline stem-progenitor fate
464 decision.

465

466 Our studies also provide evidence that innexin gap junctions not only serve as communication
467 and adhesion junctions, but that in the context of an organ system, they contribute to the
468 positioning of cells relative to each other. How might gap junctions influence the relative
469 position of the DTC and Sh1 in the distal gonad arm? The DTC also forms gap junctions with
470 germ cells, which must be disassembled as germ cells enter the bare region, only to be
471 reassembled again when in contact with Sh1 (and then again with more proximally located
472 sheath cells Sh2–5). A detailed TEM analysis of the gonad (Hall et al., 1999) led to the
473 consideration that a constant interplay of association and dissociation likely also occurs
474 between Sh1 and the underlying germ cells that move proximally along the arm: as germ cell
475 flux continually moves germ cells towards the proximal end of the gonad, the Sh1 cells
476 presumably extend their filopodia distally and form new gap junction connections with
477 incoming germ cells. Otherwise, the bare region would increase in length along the distal-
478 proximal axis.

479

480 To complement the role of gap junctions in promoting robust proliferation, the kinetics of gap
481 junction coupling between the somatic gonad and germ cells may play a role in determining the
482 strength of the interactions between the two cell types. Unlike sheath–oocyte junctions, which
483 form large plaques containing many functional gap junctions, the gap junctions formed in the
484 distal arm appear to represent looser associations of a few gap-junction channels (Starich et al.,
485 2014). Nonetheless, these associations may be sufficient to maintain adhesion with the
486 underlying germline, functioning like regularly spaced rivets, albeit dynamic and removeable
487 ones.

488

489 Disentangling the adhesive and channel functions of gap junctions is a complex issue. The
490 mutants used in this study are competent to form soma–germline gap junctions—without
491 these, germ cells fail to proliferate. However, they may form such junctions less efficiently than
492 their wild-type counterparts. For example, the pattern of localization of gap junction puncta in
493 *inx-8(rf)* and *inx-14(ag17)* appears more diffuse than in the wild type (Starich et al., 2014;

494 Starich et al., 2020). Alternatively or additionally, the mutant innexins in this study may
495 assemble into hemichannels as readily as wild-type innexins, but the pairing or opening of gap
496 junction channels may be compromised. Studies of connexin gap-junction channels in paired
497 Xenopus oocytes strongly suggest that opening of hemichannels facilitates their assembly into
498 gap junctions. That study proposed hemichannel opening collapses the intermembrane space
499 between juxtaposed cells to allow the extracellular loops of connexins to dock into gap
500 junctions (Beahm and Hall, 2004). If a similar model applies to innexin-containing gap junctions,
501 then rivet and channel function would be coupled.
502
503 How could impaired innexin function cause Sh1 to creep distally? One hypothesis is that when
504 fewer junctions are made, Sh1 cannot adhere as well to germ cells. This scenario would be
505 consistent with the observation that Sh1 is distally mispositioned when *inx-8* and *inx-9* are
506 missing from Sh1 but *inx-8(+)* is present in the DTC by virtue of heterologous expression of *inx-*
507 *8(+)* in the DTC in an *inx-8(0) inx-9(0)* double mutant (Starich et al., 2014). It is also possible that
508 the DTC and Sh1 engage in an active repellent or a passive space-excluding interaction that
509 somehow involves gap junction function. Another possibility is that a deficit in gap-junction
510 function might trigger Sh1 spreading as a means to increase the surface area over which
511 junctions may form to supply sufficient active biomolecules that transit through these
512 junctions. Nevertheless, our studies show that the position of germline stem cells is
513 independent of the position of Sh1.
514
515
516 **Acknowledgements**
517 We thank Gabriela Huelgas-Morales for discussions and constructive suggestions during the
518 course of this work, Swathi Arur for the affinity purified anti-GFP antibody, Verena Jantsch for
519 anti-pSUN-1 antibody, Edward Kipreos for anti-CYE-1 antibody. We thank Michael Cammer for
520 assistance with image analysis; the NYU Langone Microscopy Laboratory is partially supported
521 by the Cancer Center Support Grant P30CA016087. We thank WormBase. We thank Kacy

522 Gordon and the CGC, (which is funded by NIH Office of Research Infrastructure Programs P40
523 OD010440), for strains.
524
525
526 **References**
527
528 Arribere, J.A., Bell, R.T., Fu, B.X., Artiles, K.L., Hartman, P.S., Fire, A.Z., 2014. Efficient marker-
529 free recovery of custom genetic modifications with CRISPR/Cas9 in Caenorhabditis elegans.
530 Genetics 198, 837-846.
531
532 Austin, J., Kimble, J., 1987. glp-1 is required in the germ line for regulation of the decision
533 between mitosis and meiosis in C. elegans. Cell 51, 589-599.
534
535 Beahm, D.L., Hall, J.E., 2004. Opening hemichannels in nonjunctional membrane stimulates gap
536 junction formation. Biophys J 86, 781-796.
537
538 Berry, L.W., Westlund, B., Schedl, T., 1997. Germ-line tumor formation caused by activation of
539 glp-1, a Caenorhabditis elegans member of the Notch family of receptors. Development
540 (Cambridge, England) 124, 925-936.
541
542 Brodigan, T.M., Liu, J., Park, M., Kipreos, E.T., Krause, M., 2003. Cyclin E expression during
543 development in Caenorhabditis elegans. Dev Biol 254, 102-115.
544
545 Byrd, D.T., Knobel, K., Affeldt, K., Crittenden, S.L., Kimble, J., 2014. A DTC niche plexus
546 surrounds the germline stem cell pool in Caenorhabditis elegans. PLoS One 9, e88372.
547
548 Chen, J., Mohammad, A., Pazdernik, N., Huang, H., Bowman, B., Tycksen, E., Schedl, T., 2020.
549 GLP-1 Notch-LAG-1 CSL control of the germline stem cell fate is mediated by transcriptional
550 targets lst-1 and sygl-1. PLoS Genet 16, e1008650.

551

552 Cardona, A., Saalfeld, S., Schindelin, J., Arganda-Carreras, I., Preibisch, S., Longair, M.,
553 Tomancak, P., Hartenstein, V., Douglas, R. J., 2012. TrakEM2 software for neural circuit
554 reconstruction. PLoS One 7(6):e38011. doi: 10.1371/journal.pone.0038011.
555

556 Crittenden, S.L., Lee, C., Mohanty, I., Battula, S., Knobel, K., Kimble, J., 2019. Sexual dimorphism
557 of niche architecture and regulation of the Caenorhabditis elegans germline stem cell pool. Mol
558 Biol Cell 30, 1757-1769.
559

560 Dalfo, D., Ding, Y., Liang, Q., Fong, A., Cipriani, P.G., Piano, F., Zheng, J.C., Qin, Z., Hubbard,
561 E.J.A., 2020. A Genome-Wide RNAi Screen for Enhancers of a Germline Tumor Phenotype
562 Caused by Elevated GLP-1/Notch Signaling in Caenorhabditis elegans. G3 (Bethesda) 10, 4323-
563 4334.
564

565 Dejima, K., Hori, S., Iwata, S., Suehiro, Y., Yoshina, S., Motohashi, T., Mitani, S., 2018. An
566 Aneuploidy-Free and Structurally Defined Balancer Chromosome Toolkit for Caenorhabditis
567 elegans. Cell Rep 22, 232-241.
568

569 Dickinson, D.J., Ward, J.D., Reiner, D.J., Goldstein, B., 2013. Engineering the Caenorhabditis
570 elegans genome using Cas9-triggered homologous recombination. Nat Methods 10, 1028-1034.
571

572 Gordon, K.L., Zussman, J.W., Li, X., Miller, C., Sherwood, D.R., 2020. Stem cell niche exit in C.
573 elegans via orientation and segregation of daughter cells by a cryptic cell outside the niche. Elife
574 9.
575 Govindan, J.A., Nadarajan, S., Kim, S., Starich, T.A., Greenstein, D., 2009. Somatic cAMP
576 signaling regulates MSP-dependent oocyte growth and meiotic maturation in C. elegans.
577 Development 136, 2211-2221.
578

579 Hall, D.H., Hartwieg, E., Nguyen, K. C. Q, 2012. Modern Electron Microscopy Methods for *C.*
580 *elegans*. Methods in Cell Biol 107, 94-147.
581
582 Hall, D.H., Winfrey, V.P., Blaeuer, G., Hoffman, L.H., Furuta, T., Rose, K.L., Hobert, O.,
583 Greenstein, D., 1999. Ultrastructural features of the adult hermaphrodite gonad of
584 Caenorhabditis elegans: relations between the germ line and soma. Dev Biol 212, 101-123.
585
586 Henderson, S.T., Gao, D., Lambie, E.J., Kimble, J., 1994. lag-2 may encode a signaling ligand for
587 the GLP-1 and LIN-12 receptors of C. elegans. Development 120, 2913-2924.
588
589 Huang, L.S., Sternberg, P.W., 1995. Genetic dissection of developmental pathways. Methods
590 Cell Biol 48, 97-122.
591
592 Hubbard, E.J., Greenstein, D., 2000. The Caenorhabditis elegans gonad: a test tube for cell and
593 developmental biology. Dev Dyn 218, 2-22.
594
595 Hubbard, E.J.A., Schedl, T., 2019. Biology of the Caenorhabditis elegans Germline Stem Cell
596 System. Genetics 213, 1145-1188.
597
598 Kershner, A.M., Shin, H., Hansen, T.J., Kimble, J., 2014. Discovery of two GLP-1/Notch target
599 genes that account for the role of GLP-1/Notch signaling in stem cell maintenance. Proceedings
600 of the National Academy of Sciences.
601
602 Killian, D.J., Hubbard, E.J., 2005. Caenorhabditis elegans germline patterning requires
603 coordinated development of the somatic gonadal sheath and the germ line. Dev Biol 279, 322-
604 335.
605
606 Kocsisova, Z., Kornfeld, K., Schedl, T., 2019. Rapid population-wide declines in stem cell number
607 and activity during reproductive aging in C. elegans. Development 146.

608

609 Lee, C., Shin, H., Kimble, J., 2019. Dynamics of Notch-Dependent Transcriptional Bursting in Its
610 Native Context. Dev Cell 50, 426-435 e424.
611

612 Lee, C., Sorensen, E.B., Lynch, T.R., Kimble, J., 2016. C. elegans GLP-1/Notch activates
613 transcription in a probability gradient across the germline stem cell pool. eLife 5.
614

615 McCarter, J., Bartlett, B., Dang, T., Schedl, T., 1997. Soma-germ cell interactions in
616 Caenorhabditis elegans: multiple events of hermaphrodite germline development require the
617 somatic sheath and spermathecal lineages. Developmental Biology 181, 121-143.
618

619 Miyata, S., Begun, J., Troemel, E.R., Ausubel, F.M., 2008. DAF-16-dependent suppression of
620 immunity during reproduction in Caenorhabditis elegans. Genetics 178, 903-918.
621

622 Mohammad, A., Vanden Broek, K., Wang, C., Daryabeigi, A., Jantsch, V., Hansen, D., Schedl, T.,
623 2018. Initiation of Meiotic Development Is Controlled by Three Post-transcriptional Pathways in
624 Caenorhabditis elegans. Genetics 209, 1197-1224.
625

626 Nadarajan, S., Govindan, J.A., McGovern, M., Hubbard, E.J., Greenstein, D., 2009. MSP and GLP-
627 1/Notch signaling coordinately regulate actomyosin-dependent cytoplasmic streaming and
628 oocyte growth in C. elegans. Development 136, 2223-2234.
629

630 Oshima, A., Tani, K., Fujiyoshi, Y., 2016. Atomic structure of the innexin-6 gap junction channel
631 determined by cryo-EM. Nat Commun 7, 13681.
632

633 Pekar, O., Ow, M.C., Hui, K.Y., Noyes, M.B., Hall, S.E., Hubbard, E.J.A., 2017. Linking the
634 environment, DAF-7/TGFbeta signaling and LAG-2/DSL ligand expression in the germline stem
635 cell niche. Development 144, 2896-2906.
636

637 Penkner, A.M., Fridkin, A., Gloggnitzer, J., Baudrimont, A., Machacek, T., Woglar, A., Csaszar, E.,
638 Pasierbek, P., Ammerer, G., Gruenbaum, Y., Jantsch, V., 2009. Meiotic chromosome homology
639 search involves modifications of the nuclear envelope protein Matefin/SUN-1. Cell 139, 920-
640 933.
641
642 Phelan, P., 2005. Innexins: members of an evolutionarily conserved family of gap-junction
643 proteins. Biochim Biophys Acta 1711, 225-245.
644
645 Shin, H., Haupt, K.A., Kershner, A.M., Kroll-Conner, P., Wickens, M., Kimble, J., 2017. SYGL-1 and
646 LST-1 link niche signaling to PUF RNA repression for stem cell maintenance in Caenorhabditis
647 elegans. PLoS Genet 13, e1007121.
648
649 Skerrett, I.M., Williams, J.B., 2017. A structural and functional comparison of gap junction
650 channels composed of connexins and innexins. Dev Neurobiol 77, 522-547.
651
652 Starich, T., Greenstein, D., 2020. A Limited and Diverse Set of Suppressor Mutations Restore
653 Function to INX-8 Mutant Hemichannels in the Caenorhabditis elegans Somatic Gonad.
654 Biomolecules 10.
655
656 Starich, T.A., Bai, X., Greenstein, D., 2020. Gap junctions deliver malonyl-CoA from soma to
657 germline to support embryogenesis in Caenorhabditis elegans. Elife 9.
658
659 Starich, T.A., Hall, D.H., Greenstein, D., 2014. Two classes of gap junction channels mediate
660 soma-germline interactions essential for germline proliferation and gametogenesis in
661 Caenorhabditis elegans. Genetics 198, 1127-1153.
662
663 Yochem, J., Greenwald, I., 1989. glp-1 and lin-12, genes implicated in distinct cell-cell
664 interactions in C. elegans, encode similar transmembrane proteins. Cell 58, 553-563.
665

666 Zhou, Z., Hartwieg, E., Horvitz, H.R., 2001. CED-1 is a transmembrane receptor that mediates
667 cell corpse engulfment in C. elegans. Cell 104, 43-56.
668
669
670 **Materials and Methods**
671
672 *Live imaging and image analysis of live samples*
673
674 Live specimens were grown at 20°C, and staged by picking mid-L4 larvae, then allowing them to
675 grow at 20°C until imaging them 24 hours later. Animals were immobilized using 10mM
676 Levamisole (Sigma T1512) in M9 buffer. Imaging was carried out on a Nikon W1 spinning disk
677 confocal microscope. We define a biological replicate as any set of individuals collected,
678 processed and imaged together. Numbers of individuals included in each analysis is indicated in
679 the figure legends.
680
681 Image analysis was carried out on 2-dimensional maximum-projection Z-stack images of 3D
682 confocal data. The distance from the distal end of the gonad to the end of each DTC process
683 was measured along a line drawn from the end of each process parallel to the distal-proximal
684 axis to a line drawn tangent to the distal end, orthogonal to the distal-proximal axis line (Figure
685 1—figure supplement 1). The distance between the distal end of the gonad and the most distal
686 extent of Sh1 was measured in the same way. All data points were recorded for each sample
687 and used to calculate the mean values presented in Figures 1 and 2 and related figure
688 supplements.
689
690 Sh1 visualization in live worms: *bcIs39* [*lim-7p*::CED-1::GFP] (Zhou et al., 2001) encodes a
691 functional membrane-localized fusion to CED-1. *tnIs5* and *tnIs6* encode an identical non-
692 functional fusion to the first 61 amino acids of LIM-7 (*tnIs5* or *tnIs6*) denoted here as "*lim-*
693 *7p*::GFP" that includes 2.23 kb upstream, the first two exons, and the first intron of *lim-7* fused
694 to GFP (Hall et al., 1999). *inx-8(qy78[mKate2::inx-8])* is an N-terminal fusion of mKate2 to INX-8

695 generated by CRISPR-Cas9 genome editing (Gordon et al., 2020*). fasn-1(av138[fasn-1::gfp])* was
696 generated by fusing GFP to the C-terminus of FASN-1 using CRISPR-Cas9 genome editing
697 (Starich et al., 2020). *tnEX42[acy-4::gfp + rol-6(su1006)]* contains GFP fused to the ACY-4 C-
698 terminus by recombineering in the fosmid WRM061bE10 (Govindan et al., 2009). ACY-4::GFP
699 rescues the sterility of *acy-4(ok1806)* null mutants via its function in the gonadal sheath cells.
700
701
702 DTC visualization in live worms: *naIs37*[*lag-2p*::mCherry-PH] encodes mCherry fused to the PH
703 domain of rat phospholipase C delta (Pekar et al., 2017) and *qIs154*[*lag-2p*::MYR-tdTomato]
704 encodes a src kinase myristoylation sequence fused to tdTomato (Byrd et al., 2014).
705
706 *Imaris rendering of confocal images*
707
708 3D rendering of confocal stacks for Videos 1–3 was done using Imaris (Oxford Instruments, plc.
709 Abingdon, UK) according to the following algorithm for batch processing. For the Sh1 channel
710 (green): Enable Smooth = true; Surface Grain Size = 0.433 µm; Enable Eliminate Background =
711 false; Diameter Of Largest Sphere = 1.63 µm; Enable Automatic Threshold = false; Manual
712 Threshold Value = 650; Active Threshold = true; Enable Automatic Threshold B = true; Manual
713 Threshold Value B = 31622.8. For the DTC channel (red): Enable Smooth = true; Surface Grain
714 Size = 0.433 µm; Enable Eliminate Background = false; Diameter Of Largest Sphere = 1.63 µm;
715 Enable Automatic Threshold = false; Manual Threshold Value = 710; Active Threshold = true;
716 Enable Automatic Threshold B = true; Manual Threshold Value B = 14988.5.
717
718 *Strains*
719
720 *C. elegans* strains (Table S1) were grown on standard NGM media with OP50 as a food source
721 (Brenner 1974) for all figures in this work. Strain constructions employed a modified NGM
722 medium [containing 6.25 µg/ml Nystatin and 12.5 mM potassium phosphate pH 6.0 (added
723 after autoclaving) and 200 mg/ml streptomycin sulphate (added before autoclaving)] with *E.*

724 *coli* strain OP50-1 as food source. Strains were grown at 20°C. In addition to the wild-type strain
725 N2, the following alleles, described in WormBase (www.wormbase.org) or in the cited
726 references, were used:
727 Chr. I—*dpy-5(e61)* (Brenner 1974), *inx-14(ag17)* (Miyata et al., 2008; Starich et al., 2014), *unc-*
728 *13(e51)* (Brenner 1974), *fasn-1(av138[fasn-1::gfp])* (Starich et al. 2020), *sygl-*
729 *1(q983[3xOLLAS::sygl-1])* (Shin et al., 2017), *unc-54(e190)* (Brenner 1974).
730 Chr. IV—*inx-8(qy78[mKate2::inx-8])* (Gordon et al., 2020) , *inx-8(qy78 tn2031)* (this work), *inx-*
731 *8(tn2034)* (this work), *inx-8(tn2075)* (this allele was generated on the *tmC5* balancer
732 chromosome, this work), *inx-9(ok1502), inx-8(qy102[mKate2::inx-8)] inx-9(ok1502)* (Gordon et
733 al., 2020), *inx-8(tn1513tn1553) inx-9(ok1502)* (Starich and Greenstein, 2020), *inx-*
734 *8(tn1513tn1555) inx-9(ok1502)* (Starich et al., 2020), *dpy-20(e1282)* (Hosono et al. 1982).
735 Chr. V—*acy-4(ok1806)* (Govindan et al. 2009).
736 Balancer chromosomes (Dejima et al., 2018) used included: *tmC18 [dpy-5(tmIs1236)]* I,
737 *tmC27[tmIs1239]* I, *tmC5[tmIs1220]* IV.
738 Integrated transgenes included: *naIs37[lag-2p::mCherry::plcdeltaPH + unc-119(+)]* I (Pekar et
739 al., 2017), *mIs11[myo-2p::gfp + pes-10p::gfp + gut promoter::gfp]* IV, *bcIs39[lim-7p::ced-1::gfp +*
740 *lin-15(+)]* V (Zhou *et al*., 2001), *qIs154[lag-2p::MYR::tdTomato +ttx-3p::gfp]* V (Byrd et al., 2014),
741 *tnIs5[lim-7p::gfp + rol-6(su1006)]* X*, tnIs6[lim-7p::gfp + rol-6(su1006)]* X (Hall et al., 1999),
742 *cpIs122[lag-2p::mNeonGreen::plcdeltaPH]* (Gordon et al., 2020).
743 Extrachromosomal arrays used included: *tnEx42[acy-4::gfp + rol-6(su1006)]* (Govindan et al.,
744 2009).
745
746 **Table S1. Strains used in this study**

	Strain	Genotype	Reference
747			
748	**AG400**	*fasn-1(av138[fasn-1::gfp]) I*	(Starich et al. 2020)
749	**CB190**	*unc-54(e190) I*	(Brenner 1974)
750	**CB1282**	*dpy-20(e1282) IV*	(Hosono et al. 1982)
751	**DG2506**	*acy-4(ok1806) V; tnEx42[acy-4::gfp + rol-6(su1006)]*	(Govindan et al. 2009)
752	**DG4959**	*qIs154[lag-2p::MYR::tdTomato + ttx-3p::gfp] V;*	

	tnIs5[lim-7p::gfp + rol-6(su1006)] X	(this work)
DG4977	*inx-14(ag17) I; qIs154[lag-2p::MYR::tdTomato + ttx-3p::gfp] V; tnIs5[lim-7p::gfp + rol-6(su1006)] X*	(this work)
DG5020	*naIs37[lag-2p::mCherry::PH + unc-119(+)] I; bcIs39[lim-7p::ced-1::gfp + lin-15(+)] V*	(this work)
DG5026	*inx-14(ag17) naIs37[lag-2p::mCherry::PH + unc-119(+)] I; bcIs39[lim-7p::ced-1::gfp + lin-15(+)] V*	(this work)
DG5027	*naIs37[lag-2p::mCherry::PH + unc-119(+)] I; inx-9(ok1502) IV; bcIs39[lim-7p::ced-1::gfp + lin-15(+)] V*	(this work)
DG5029	*naIs37[lag-2p::mCherry::PH + unc-119(+)] I; inx-8(tn1513tn1555) inx-9(ok1502) IV; bcIs39[lim-7p::ced-1::gfp + lin-15(+)] V*	(this work)
DG5059	*inx-9(ok1502) IV*	(this work)
DG5063	*inx-8(qy78[mKate2::inx-8]) IV*	(this work)
DG5064	*inx-8(qy102(mKate2::inx-8)) inx-9(ok1502) IV*	(this work)
DG5070	*inx-14(ag17) I; inx-8(qy78[mKate2::inx-8]) IV*	(this work)
DG5131	*naIs37[lag-2p::mCherry::PH + unc-119(+)] I;inx-8(qy78[mKate2::inx-8]) IV; bcIs39[lim-7p::ced-1::gfp + lin-15(+)] V*	(this work)
DG5133	*naIs37[lag-2p::mCherry::PH + unc-119(+)] I; inx-8(qy102(mKate2::inx-8)) inx-9(ok1502) IV; bcIs39[lim-7p::ced-1::gfp + lin-15(+)] V*	(this work)
DG5136	*sygl-1(q983[3xOLLAS::sygl-1]) naIs37[lag-2p::mCherry::PH + unc-119(+)] I; bcIs39[lim-7p::ced-1::gfp + lin-15(+)] V*	(this work)
DG5150	*inx-14(ag17) sygl-1(q983[3xOLLAS::sygl-1]) naIs37[lag-2p::mCherry::PH + unc-119(+)] I; bcIs39[lim-7p::ced-1::gfp + lin-15(+)] V*	(this work)
DG5181	*sygl-1(q983[3xOLLAS::sygl-1]) naIs37[lag-2p::mCherry::PH + unc-119(+)] I; inx-8(qy78[mKate2::inx-8]) IV; bcIs39[lim-7p::ced-1::gfp + lin-15(+)] V*	(this work)
DG5229	*naIs37[lag-2p::mCherry::PH + unc-119(+)] I; inx-8(qy78tn2031) IV; bcIs39[lim-7p::ced-1::gfp + lin-15(+)] V*	(this work)
DG5232	*naIs37[lag-2p::mCherry::PH + unc-119(+)] I; inx-8(tn2034) IV;*	

	bcIs39[lim-7p::ced-1::gfp + lin-15(+)] V	(this work)
DG5248	*sygl-1(q983[3xOLLAS::sygl-1]) naIs37[lag-2p::mCherry::PH + unc-119(+)] I; inx-8(qy78tn2031) IV; bcIs39[lim-7p::ced-1::gfp + lin-15(+)] V*	(this work)
DG5249	*sygl-1(q983[3xOLLAS::sygl-1]) naIs37[lag-2p::mCherry::PH + unc-119(+)] I; inx-8(tn2034) IV; bcIs39[lim-7p::ced-1::gfp + lin-15(+)] V*	(this work)
DG5250	*inx-8(qy78tn2031) IV*	(this work)
DG5251	*inx-8(tn2034) IV*	(this work)
DG5270	*inx-14(ag17) I*	(this work)
DG5310	*naIs37[lag-2p::mCherry::PH + unc-119(+)] I; acy-4(ok1806) V; tnEx42[acy-4::gfp + rol-6(su1006)]*	(this work)
DG5320	*fasn-1(av138[fasn-1::gfp]) naIs37[lag-2p::mCherry::PH + unc-119(+)] I*	(this work)
DG5346	*naIs37[lag-2p::mCherry::PH + unc-119(+)] I; inx-8(qy78[mKate2::inx-8])/tmC5[tmIs1220] IV; bcIs39[lim-7p::ced-1::gfp + lin-15(+)] V*	(this work)
DG5347	*naIs37[lag-2p::mCherry::PH + unc-119(+)] I; inx-8(qy78tn2031)/tmC5[tmIs1220] IV; bcIs39[lim-7p::ced-1::gfp + lin-15(+)] V*	(this work)
DG5357	*tmC5[tmIs1220] inx-8(tn2075) IV*	(this work)
DG5366	*naIs37[lag-2p::mCherry::PH + unc-119(+)] I; inx-8(qy78[mKate2::inx-8])/tmC5[tmIs1220] inx-8(tn2075) IV; bcIs39[lim-7p::ced-1::gfp + lin-15(+)] V*	(this work)
DG5367	*inx-14(ag17) fasn-1(av138[fasn-1::gfp]) naIs37[lag-2p::mCherry::PH + unc-119(+)] I*	(this work)
DG5378	*fasn-1(av138[fasn-1::gfp]) naIs37[lag-2p::mCherry::PH + unc-119(+)] I; inx-8(qy78[mKate2::inx-8]) IV*	(this work)
DG5380	*bcIs39[lim-7p::ced-1::gfp + lin-15(+)] V*	(this work)
FX30140	*tmC5[tmIs1220] IV*	(Dejima et al. 2018)
JK1466	*gld-1(q485)/dpy-5(e61) unc-32(e51) I*	(Francis et al. 1995)

811 **KLG006** *inx-8(qy78[mKate2::inx-8]) IV; tnIs6[plim-7::gfp + rol-6(su1006)] X;*
812 *cpIs122(lag-2p::mNeonGreen::plcdeltaPH)* (Gordon et al., 2020)
813 **NK2571** *inx-8(qy78[mKate2::inx-8]);*
814 *cpIs122 [lag-2p::mNeonGreen::plcdeltaPH]* (Gordon et al., 2020)
815 **NK2576** *inx-8(qy102(mKate2::inx-8)) inx-9(ok1502);*
816 *cpIs122(lag-2p::mNeonGreen::plcdeltaPH)* (Gordon et al., 2020)
817
818 *Strain constructions*
819
820 Multiply mutant strains were constructed in a straightforward manner (Huang and Sternberg,
821 1995). *tmC18* was used as a balancer chromosome for *inx-14(ag17)*. *tmC27* was used as a
822 balancer chromosome for *sygl-1(q983)*. *tmC5* (or the derivatives described) or *mIs11* were used
823 as balancer chromosomes for *inx-8* and *inx-9* mutant alleles. The presence of *inx-14(ag17)* in
824 strains was verified by PCR and DNA sequencing. The *ag17* allele was originally described as an
825 Arg to His change in the second extracellular loop of INX-14, but the exact residue position was
826 not specified (Miyata et al., 2008). A 1.2-kb PCR fragment covering this region was amplified
827 with primers inx-14delF and inx-14delR (see Table S2 for the sequence of oligonucleotides used
828 in this study). The PCR fragment was sequenced with the inx-14delR primer. No sequence
829 changes were found in Arg residues predicted to occupy the second extracellular loop.
830 However, a CGT to CAT (R326H) change was identified at a residue position predicted to lie near
831 the cytoplasmic end of the fourth transmembrane domain, and we surmise that this change
832 represents the original *ag17* mutation. The presence of the *sygl-1(q983[3xOLLAS::sygl-1])*
833 mutation in strains was verified by PCR with primers sygl1-F and sygl1-R, which produce a 216
834 bp product in the wild type and a 348 bp product in *sygl-1(q983)* and by anti-OLLAS staining.
835 The presence of *inx-8(qy78tn2031)* and *inx-8(tn2034)* in strains was verified by PCR with
836 oligonucleotide primers inx8_delta.F and inx8_delta.R. To construct DG5367 *inx-14(ag17) fasn-*
837 *1(av138[fasn-1::gfp]) naIs37 I, fasn-1(av138[fasn-1::gfp]) naIs37/dpy-5(e61) unc-13(e51)*
838 heterozygotes were generated and Dpy non-Unc recombinants were sought, which resulted in
839 the isolation of a *dpy-5(e61) fasn-1(av138[fasn-1::gfp]) naIs37 I* intermediate strain. From, *inx-*

840 *14(ag17)/dpy-5(e61) fasn-1(av138[fasn-1::gfp]) naIs37* heterozygotes, recombinants of
841 genotype *inx-14(ag17) fasn-1(av138[fasn-1::gfp]) naIs37/dpy-5(e61) fasn-1(av138[fasn-1::gfp])*
842 *naIs37* were identified by virtue of their increased GFP signal using a fluorescence dissecting
843 microscope. The presence of *inx-14(ag17)* in the desired recombinants was verified by DNA
844 sequencing. *naIs37* was shown to be tightly linked to *unc-54(e190)* on the right end of LGI as
845 follows. From *dpy-5(e61) fasn-1(av138[fasn-1::gfp]) naIs37/unc-54(e190)* heterozygotes, of 15
846 *unc-54(e190)* homozygotes, none contained the *naIs37* marker (4 were recombinants
847 expressing *fasn-1::gfp*). Of 38 wild-type segregants of the aforementioned parental
848 heterozygous strain, all expressed the *naIs37* marker (11 were recombinants lacking *fasn-1::gfp*
849 expression). DG5380 was derived from DG5020 by crossing to N2 males and segregating away
850 *naIs37*; the *bcIs39* source was MD701, available from the CGC.
851
852 *Electron microscopy methods and analysis*
853
854 Wild-type N2 young adults were analyzed using high-pressure freezing/freeze-substitution
855 freezing (HPF/FS; Hall et al., 2012). Four animals from chemical immersion and four animals
856 from HPF/FS were collected in serial sections on slot grids, ranging from 80 nm–100 nm
857 thickness on an RMC PowerTome XL ultramicrotome (Eden Instruments, Valence, France).
858 Sections were post-stained in 2% uranyl acetate in H_2O for 20 min and in Reynold's lead for 3
859 min. Sections from each animal were viewed in the gonad region using Digital Micrograph
860 software (Gatan, Pleasanton, CA) for the JEOL JEM-1400Plus M (Jeol USA, Peabody, MA), using
861 a Gatan Orius SC1000B digital camera.
862
863 We selected the most optimally positioned and resolved HPF/FS-fixed animal (2% osmium
864 tetroxide, 0.1% uranyl acetate, and 2% H_2O in acetone) to collect high-resolution montages of
865 the gonad arm from every third section covering 80 µm, including the DTC and sheath filopodia
866 of a posterior distal gonad arm. This series was collected from the tail to the vulva region to
867 encompass the whole posterior gonad arm, but we did not collect full images closer to the
868 gonad reflection in order to save effort and expense. The pixel size for the images was 3.23 nm.

869 The images were aligned with TrakEM2 software (Cardona et al., 2012) and traced on a Wacom
870 DTZ 2100D tablet (Wacom, Portland, OR) to build the 3D model.
871
872 We followed the DTC processes and their fragments and the filopodial extensions of Sh1 due to
873 their increased translucency compared with the germ cells and by the fact that these somatic
874 cellular extensions contained many small mitochondria (Video 4). We observed what we infer
875 to be shed pieces of the DTC beginning at approximately 30 µm from the distal end, as has been
876 observed using light microscopic methods (Byrd et al., 2014). However, some DTC and Sh1
877 processes may appear discontinuous due to the fact that micrographs of every third section
878 were used to generate the reconstructed model (Video 5). Regardless of the effect that this
879 sampling technique has on our ability to resolve contiguous versus shed bits of somatic gonadal
880 cells, this TEM analysis is in agreement with our light microscopic observations that a large
881 subset of distal germ cell progenitors are not in contact either with the DTC or Sh1.
882
883 *Brood counts and Embryonic lethality measurements*
884
885 Because *inx-8(qy78[mKate2::inx-8])* brood counts and embryonic lethality were highly variable,
886 we used a single batch of NGM media with OP50 food source for all brood count measurements
887 reported in Table 1. To prevent mold formation, the medium contained 6.25 µg/ml Nystatin. L4-
888 stage hermaphrodites were cultured individually on 35 mm Petri plates and transferred
889 approximately every 24 hours until they stopped producing embryos (4–6 days). Worms that
890 crawled off the media and died were redacted (varied from 0–10% depending on the
891 experiment). Embryos that failed to hatch after 24–36 hours were counted and scored as dead.
892 In the majority of cases, these embryos exhibited morphological abnormalities. Control
893 experiments demonstrated that these embryos were not simply delayed and never hatched.
894 Embryos that hatched were counted and scored as viable.
895
896 *Genome editing*
897

898 CRISPR-Cas9 genome editing was used to generate *inx-8* null alleles in both the *inx-*
899 *8(qy78[mKate2::inx-8])* and wild-type genetic backgrounds. The approach taken generated
900 identical 1525 bp deletions within the *inx-8* locus in both genetic backgrounds starting 136 bp
901 upstream of the wild-type *inx-8* ATG start codon and extending 221 bp into *inx-8* exon 3. In the
902 *inx-8(qy78[mKate2::inx-8])* context, this edit removes both the mKate2 moiety and *inx-8*. The
903 deletions are expected to constitute *inx-8* null alleles because, in addition to removing the start
904 codon, they delete amino acids 1–349 (out of 382 amino acids), including virtually all residues
905 essential for spanning the plasma membrane and forming a channel (Starich and Greenstein,
906 2020). The approach used pRB1017 to express two single guide RNAs (sgRNAs) under control of
907 the *C. elegans* U6 promoter (Arribere et al., 2014). Oligonucleotides inx8_us_sgRNA1.F and
908 inx8_us_sgRNA1.R were annealed and used to generate the plasmid inx8_us_sgRNA1 to direct
909 Cas9 cleavage 136 bp upstream of the ATG initiator codon (Table S2 lists all oligonucleotides
910 used in this study). Oligonucleotides inx8_sgRNA1.F and inx8_sgRNA1.R were annealed and
911 used to generate the plasmid inx8_sgRNA1 to direct Cas9 cleavage in exon 3. To generate
912 sgRNA clones, annealed oligonucleotides were ligated to *Bsa*I-digested pRB1017 plasmid vector,
913 and the resulting plasmids were verified by Sanger sequencing. pDD162 served as the source of
914 Cas9 expressed under control of the *eef-1A.1/eft-3* promoter (Dickinson et al., 2013). The repair
915 template oligonucleotide used was inx8_rpr. Genome editing employed the *dpy-10* co-
916 conversion method (Arribere et al., 2014). The injection mix contained pJA58 (7.5 ng/µl), AF-ZF-
917 827 (500 nM), inx8_us sgRNA1 (25 ng/µl), inx8_sgRNA1 (25 ng/µl), inx8_rpr (500 nM), and
918 pDD162 (50 ng/µl) and was injected into adult hermaphrodites from strains DG5131 *naIs37[lag-*
919 *2p::mCherry::PH + unc-119(+)] I; inx-8(qy78[mKate2::inx-8]) IV; bcIs39[lim-7p::ced-1::gfp + lin-*
920 *15(+)] V* and DG5020 *naIs37[plag-2::mCherryPH + unc-119(+)] I; bcIs39[lim-7p::ced-1::gfp + lin-*
921 *15(+)]V*. Correct targeting was verified by conducting PCR with primer pairs inx8_delta.F and
922 inx8_delta.R followed by DNA sequencing. Three deletion alleles were recovered from the
923 injections into DG5131 *(qy78tn2031, qy78tn2032,* and *qy78tn2033)*, and two deletion alleles
924 were recovered from the injections into DG5020 *(tn2034* and *tn2035)*. The deletion alleles were
925 outcrossed to *naIs37[lag-2p::mCherryPH +unc-119(+)]/+ I; tmC5(tmIs1220[myo-2p::Venus])/+*
926 *IV; bcIs39[lim-7p::ced-1::gfp + lin-15(+)/+ V* males to generate DG5229 and DG5232.

927 Homozygous strains were analyzed by confocal microscopy. To introduce an *inx-8* null allele
928 onto the *tmC5[tmIs1220]* IV balancer chromosome, the same injection mix of CRISPR reagents
929 as described above was injected into *dpy-20(e1282)/tmC5[tmIs1220]* IV heterozygotes. The *inx-*
930 *8(tn2075)* null allele was generated on the balancer chromosome, which resulted from a 1526
931 bp deletion that differed from the other CRISPR-generated *inx-8* null alleles by the removal of
932 an extra base at the cut site.
933
934 **Table S2. Oligonucleotides used in this study**

Oligo name	Sequence
AF-ZF-827	CACTTGAACTTCAATACGGCAAGATGAGAATGACTGGAAACCGTACCGCATGCGGTGCCTATGGTAGCGGAGCTTCACATGGCTTCAGACCAACAGCCTAT (Arribere et al., 2014)
inx8_us_sgRNA1.F	TCTTGTGGAAAACAGAGGAATGGG
inx8_us_sgRNA1.R	AAACCCCATTCCTCTGTTTTCCAC
inx8_sgRNA1.F	TCTTGAGTGACTTGGTAGCATCGG
inx8_sgRNA1.R	AAACCCGATGCTACCAAGTCACTC
inx8_RPR	GGTGGCCAATAAAAATGCTTTTCTTTTTGCTTTTCTCTATCTACTTCCGTTCCGCCCCGGAGGTTGCCGTGGAGATGTACAGCGACTTTTTAGTAAGTCTTTTCAAC
inx8_delta.F	CCTTCGACCTGATTTCCCCTTCTTCTAATG
inx8_delta.R	CTATTGCTTTCCGTTCTTCAAGATGTTGTTG
inx-14delF	GATACGACGTGAGCAATGGAACGTC
inx-14delR	CTTGGACTTGAAGTGAGAGTTGGAG
sygl1-F	ATCATCGAACCATTGTCATCACGC
sygl1-R	TTTGCCTTGATCTCCAAGTGTTGC

953
954
955 *Immunostaining and image analysis of fixed samples*
956

957 Immunostaining was carried out as described (Mohammad et al., 2018). Briefly, synchronized
958 adult hermaphrodites, 24-hr past mid-L4, were dissected in PBST (PBS with 0.1% Tween 20),
959 with 0.2 mM levamisole to extrude the gonads. The gonads were fixed in 3% paraformaldehyde
960 solution for 10 min and then post-fixed in −20° chilled methanol for 10 min. After 3x 10-min
961 washes with PBST, they were blocked in 30% goat serum for 30 min at RT. The gonads were
962 then incubated with the desired primary antibodies diluted (see below) in 30% goat serum at 4°
963 overnight. The next day, after 3x 10-min PBST washes, the gonads were further incubated with
964 appropriate secondary antibodies, diluted in 30% goat serum, at 4° overnight. The gonads were
965 washed 3 times with PBST, then incubated with 0.1 g/ml DAPI in PBST for 30 min. After removal
966 of excess liquid, the gonads were mixed with anti-fading agent (Vectashield) and transferred to
967 an agarose pad on a slide. Hyperstack images were captured using a spinning disk confocal
968 microscope (PerkinElmer-Cetus, Norwalk, CT). Two overlapping hyperstack images were
969 captured for each gonad arm to obtain coverage of >50 cell diameters from the distal end of
970 the gonad. Images were further processed in Fiji, and DAPI stained nuclei were used to mark
971 the number of cell diameters from the distal end. Employing pixel to micron ratio, specific to
972 the images captured, cell diameters were converted into microns where required.
973
974 SYGL-1-positive zone length assessment: OLLAS staining was used to assess 3xOLLAS::SYGL-1
975 accumulation (Shin et al., 2017). In wild-type young adults, SYGL-1 accumulates at the distal end
976 of the germline and is downregulated around 10 cell diameters from the distal tip (Kocsisova et
977 al., 2019; Shin et al., 2017). Cell diameters were counted from the distal end of the germline up
978 to the row where SYGL-1 is no longer visible by eye. OLLAS staining in the wild-type worms
979 without OLLAS tag was used to differentiate staining from the background. To confirm the
980 accuracy of our visual assessment, we quantified the intensity of SYGL-1 accumulation in the
981 distal germline, employing methods similar to Chen et al., 2020 in the same set of germlines
982 where the SYGL-1 zone was visually evaluated. We found that the cell diameter position called
983 as the end of the SYGL-1 zone consistently corresponded to 6–9% of peak SYGL-1 intensity, for
984 each genotype (Figure 3—figure supplement 2). These results indicate that the SYGL-1 zone
985 length visual assessment was reproducible and consistent.

986

987 Progenitor zone length assessment: The gonads were stained with a progenitor zone marker,
988 anti-CYE-1, and an early meiotic prophase marker, pSUN-1, (anti-SUN-1 S8-Pi) (Mohammad et
989 al., 2018). For assessing the progenitor zone length, cell diameters (rows) were counted from
990 the distal end of the germline, where all cells are CYE-1-positive, until the point after which the
991 majority of the cells in a row have switched from staining for CYE-1 to pSUN-1. Note that pSUN-
992 1 staining is not shown in the figures though it was used to assess the PZ border.
993
994 Assessment of distal position of Sh1: anti-GFP antibody staining was used to visualize the
995 sheath, where cell diameters were counted from distal end to the point where GFP staining
996 became prominent.
997
998 To quantify the distance from the distal end to the border of expression of any protein, we have
999 used either ~30 gonads for single-replicate experiments and ~20 gonads for multi-replicate
1000 experiments. We define a biological replicate as independently dissected and stained, along
1001 with the controls in the same tube, and images acquired with the same settings. During these
1002 experiments, no outliers were encountered. In rare cases, acquired images, which either failed
1003 to stitch by Fiji or had poor staining, were discarded.
1004
1005 Primary antibodies used: mouse anti-CYE-1 (1:100; (Brodigan et al., 2003)); guinea pig anti-SUN-
1006 1 S8-Pi (1:1000; (Penkner et al., 2009)); rat anti-OLLAS (1:2000; Novus Biological); rabbit anti-
1007 GFP (1:200; from Swathi Arur, MD Anderson Cancer Center); and rabbit anti-INX-8 (1:25; Starich
1008 et al., 2014)
1009
1010 Secondary antibodies used: Alexa Fluor 647 goat anti-mouse (Life Technologies, Carlsbad, CA);
1011 Alexa Fluor 594 goat anti-guinea pig (Invitrogen, Waltham, MA), Alexa Fluor 594 donkey anti-rat
1012 (Invitrogen); and Alexa Fluor 488 goat anti-rabbit (Invitrogen).
1013
1014

Funding

ACS grant PF-19-231-01-CSM to TT

NIH R35GM134876 and R01AG065672 to EJAH

R01 GM100756 to T. Schedl

NIH R01GM57173 and R35GM144029 to DG

NIH Office of the Director R24OD10943 to DHH

NIH P30HD071593 and 1S10OD016214-01A1 supports electron microscopy in DHH lab.

Contributions

TT, EJAH, wrote the manuscript with contributions from all authors.

TT, AM, DG, T Starich performed, analyzed, and interpreted experiments.

EJAH, T Schedl, DG oversaw experiments and analysis

DHH designed and supervised TEM studies and the data analysis.

KCQN conducted TEM studies and 3D reconstructions.

Competing interests

E.J.A.H. holds US patent 6,087,153.

1036 **Figure Legends**

1037

1038 **Figure 1.** Germline and somatic gonad innexins are required for proper somatic gonad
1039 architecture. A. Schematic of paired somatic and germline octameric hemichannels. B.
1040 Schematic diagram of the *inx-8 inx-9* locus and the *inx-14* locus, with relevant mutations
1041 indicated in red. C. Fluorescent confocal maximum projection images of distal gonads in live
1042 worms. Distal tip cell (DTC) marked in magenta (*naIs37[lag-2p::mCherry-PH]*) and sheath pair 1
1043 (Sh1) marked in green (*bcIs39[lim-7p::CED-1::GFP])*. Top: strain bearing markers only, denoted
1044 "wild-type", representative of phenotypic Classes 1 and 2. D. *inx-14(ag17)* and *inx-*
1045 *8(tn1513tn1555) inx-9(ok1502)*, denoted "*inx-8(rf)*" after Starich et al. (2020), representative of
1046 Class 3. E. Diagram of DTC–Sh1 relationship in distal end of a typical wild-type gonad (DTC
1047 magenta, Sh1 green) for phenotypic Classes 1–3. Class 1: greater than 8 µm (two cell diameters)
1048 separates the proximal most extent of the DTC (vertical line topped with magenta dot) and the
1049 distal most border of Sh1 (vertical line topped with green dot) as measured in slice-by-slice
1050 analysis of Z series; Class 2: ≤8 µm separates DTC and Sh1 extensions or interdigitation of DTC
1051 and Sh1 is seen up to the position of the average DTC process length (vertical line topped with
1052 blue dot); Class 3: distal position of Sh1 is distal to the average DTC process length. A diagram of
1053 all measurements taken for live fluorescent images is shown in Figure 1—figure supplement 1.
1054 F. The proportion of gonads examined that fall into the phenotypic classes indicated. G. Plot
1055 showing the distance between the average DTC process length (blue dots), the longest DTC
1056 process (magenta dots) and the distal-most border of Sh1 (green dots); each trio of dots joined
1057 by a dark blue line represents the data for a single gonad, analyzed as a confocal maximum
1058 projection. Scale bars are 10 µm. Strains used are DG5020, DG5026 and DG5029. See Table S1
1059 for complete genotypes.

1060

1061

1062 **Video 1.** Confocal stack and 3D rendering of representative Class 1 gonad. Strain DG5020.
1063 **Video 2.** Confocal stack and 3D rendering of representative Class 2 gonad. Strain DG5020.
1064 **Video 3.** Confocal stack and 3D rendering of representative Class 3 gonad. Strain DG5026.

1065

1066

1067 **Figure 1—figure supplement 1.** Consistent trends in Sh1 and DTC positions are observed with
1068 multiple markers.
1069 A. Schematic diagram of DTC and Sh1 parameters measured. Each black dot represents a point
1070 in a maximum projection Z-stack for which the distance from the distal end was measured in
1071 microns. B. Fluorescent micrographs of gonads in live worms bearing indicated markers that
1072 label DTC (magenta lettering) or Sh1 (green lettering), in wild-type and *inx-14(ag17)* mutant
1073 backgrounds, as indicated: *naIs37*, *bcIs39*, *qIs154*, and *tnIs5* are integrated transgenes; *tnEx42*
1074 carries a rescuing *acy-4p*::*gfp* fusion on an extrachromosomal array; and *fasn-1(av138[fasn-*
1075 *1::gfp])* was tagged at the endogenous locus using CRISPR-Cas9 genome editing (see Table S1
1076 for full genotypes). The *fasn-1* and *acy-4* fusions also drive expression in non-gonadal tissues. C.
1077 The proportion of gonads examined that fall into the phenotypic classes indicated. D. Plot
1078 showing the distance between the average DTC process length (blue dots), the longest DTC
1079 process (magenta dots) and the distal-most border of Sh1 (green dots); each trio of dots joined
1080 by a dark blue line represents the data for a single gonad. E. Plots showing quantitative
1081 measurement of parameters diagrammed in (A). Although the behavior of the DTCs marked by
1082 different markers is variable, and DTCs marked with *qIs154* show significantly longer DTC
1083 processes, the behavior of Sh1 in the presence of either marker shows significantly consistent
1084 changes across mutant genotypes. All p-values result from Student's *t*-test. Scale bars are 10
1085 µm. Strains used were DG5020, DG4959, DG4977, DG5026, DG5320, DG5367, DG5310. See
1086 Table S1 for complete genotypes.

1087

1088

1089 **Figure 1—figure supplement 2.** Snapshot of transmission electron micrograph (TEM)
1090 reconstruction and guide to Videos 4 and 5.

1091

1092 **Video 4.** Serial thin section movie of every third section from the DTC to the distal extensions of
1093 Sh1 in a young adult hermaphrodite posterior gonad arm. Germ cell nuclei are marked in yellow

1094 if the corresponding germ cells receive direct contact from a DTC or Sh1 process, or in salmon if
1095 they do not. The soma and processes of the DTC are filled in pink. Filopodial extensions of the
1096 somatic sheath are filled in green. Individual images are composed from multi-panel montages
1097 (mostly 3 x 4 montages). Scale bar is 3 µm. Video 4 is available at
1098 https://datadryad.org/stash/share/CgAYZh4cDADyskEuMQwsWj_3f93PSl9_ETgna-uVRYI
1099 or at https://s3.msi.umn.edu/greenste/Video4_R1.avi
1100
1101 **Video 5.** Model of the distal gonad. The DTC, its processes and fragments are in pink. Nearest
1102 sheath cell bodies lie out of frame proximally, but their filopodial extensions are shown in
1103 green, extending towards the DTC. Germ cell nuclei are modelled as spheres; the nuclei of
1104 those germ cells that do not come in contact with either DTC or Sh1 are colored in salmon,
1105 while germ cells with direct contact are shown in yellow. The true volume of each germ cell is
1106 larger than is shown here because each sphere is centered only on the cell nucleus. Scale bar is
1107 5 µm.
1108
1109
1110 **Figure 2.** N-terminal fusion of mKate2 to INX-8 generates an INX-8 protein that alters somatic
1111 gonad morphology. A. Schematic diagram showing the genetic manipulations used in this
1112 section. *inx-8(qy78[mKate2::inx-8])* was created by placing mKate2 in-frame with the N-
1113 terminus of INX-8 (Gordon et al., 2020). *inx-8(qy78tn2031)* was created by deleting the *inx-8*
1114 coding region and mKate2 moiety in the *inx-8(qy78)* background. B. Representative distal
1115 gonads stained with anti-INX-8 antibody; Top: N2 wild-type, Bottom: DG5063 *inx-*
1116 *8(qy78[mKate2::inx-8]).* C. Dot plot with overlaid quantile box plots showing the distance from
1117 the distal end of the gonad to the Sh1 distal border for each genotype. Each dot represents a
1118 single gonad of that genotype. P-value was calculated using Student's *t*-test. D. Fluorescent
1119 micrographs of live animals with the DTC marked by *naIs37[lag-2p::mCherry-PH]* and Sh1
1120 marked by *bcIs39[lim-7p::ced-1::gfp]*. Top: wild-type with markers only. Middle: *inx-*
1121 *8(qy78[mKate2::inx-8])*. Bottom: *inx-8(qy78tn2031).* E. Quantitative dot-plots as in Figure 1;
1122 data for wild-type (marker only) strain in E is the same as in Figure 1. Each pair of dots

1123 connected by a line represents data from a single gonad. Scale bar 10µm. Strains used were N2,
1124 DG5063, DG5020, DG5131, DG5229, DG5320, DG5378. See Table S1 for complete genotypes.
1125
1126 **Figure 2—figure supplement 1.** Detection of INX-8 antibody overlaps with mKate2 fluorescence
1127 in *inx-8(qy78[mKate2::inx-8)]*. Representative image of dissected distal gonad stained with
1128 anti-INX-8 antibody (top, green), mKate2 fluorescence (middle, red) and merged (bottom,
1129 yellow) in DG5063 *inx-8(qy78[mKate2::INX-8])*. The distal end of the gonad is on the left. In all
1130 gonads examined (n=32), overlap was complete. Scale bars are 10 µm.
1131
1132 **Figure 2—figure supplement 2.** The *inx-8(qy78[mKate2::inx-8)* allele behaves as a dosage-
1133 sensitive antimorph. A. Schematic diagram showing additional relevant alleles at the *inx-8* and
1134 *inx-9* loci. B–E. Relevant genotypes are given for *inx-8* and *inx-9* only. All strains also contain
1135 *naIs37* to mark the DTC and *bcIs39* to mark Sh1. *inx-8(qy78[mKate2::inx-8])* and *inx-*
1136 *8(qy102[mKate2::inx-8])* are abbreviated as *inx-8(qy78)* and *inx-8(qy102)* to aid comparisons
1137 between genotypes. B. Representative fluorescent micrographs of live worms carrying each
1138 relevant allele, as indicated (images for *inx-8(+), inx-8(qy78[mKate2::inx-8])* and *inx-*
1139 *8(qy102tn2031)* are the same as in Fig. 2B, included here for comparison). C. Stacked histogram
1140 showing the frequency of each of the phenotypic classes described in Fig. 1, for each genotype,
1141 as indicated. D. Table showing frequency of Class 3 gonads for each genotype, with indicated
1142 pairwise significance levels derived from a Fisher's Exact Test. E. Quantitative plots showing
1143 changes to DTC morphology and Sh1 position. All p-values result from Student's *t*-test. Scale
1144 bars are 10 µm. Strains used were DG5020, DG5131, DG5229, DG5232, DG5027, DG5133,
1145 DG5346, DG5347, DG5366. See Table S1 for complete genotypes.
1146
1147 **Figure 2—figure supplement 3.** Direct comparison of *inx-8(qy78[mKate2::inx-8]* and *lim-7p-*
1148 driven transgenes as markers for Sh1. A. Individual gonads carrying different Sh1 markers in
1149 addition to *inx-8(qy78[mKate2::inx-8]).* Left, top to bottom: Individual channels and merged
1150 image of a single worm co-expressing the DTC marker *cpIs122[lag-2p::gfp], inx-*
1151 *8(qy78[mKate2::inx-8])* and the sheath cell marker *tnIs5[lim-7p::gfp]*. Right, top to bottom:

1152 Individual channels and merged image of a single worm co-expressing the DTC marker
1153 *naIs37[lag-2p::mCherry-PH]*, *inx-8(qy78[mKate2::inx-8])* and the sheath cell marker *bcIs39[lim-*
1154 *7p::ced-1::gfp]*. B. Two individual gonads of the same genotypes as in (A), showing incomplete
1155 overlap between mKate2::INX-8 and the respective GFP sheath cell markers. White arrowheads
1156 mark the most distal extent of each marker in the single-channel panels. C and D: *inx-*
1157 *8(qy78[mKate2::inx-8]* is abbreviated as "*inx-8(qy78)".* C. Frequency of overlap. Of 46 gonads
1158 examined, 39 showed perfect overlap as shown in these images. D. Proportion of gonads in
1159 phenotypic Classes 1–3 as scored by mKate2 or as scored by GFP expression, as indicated by
1160 bold in the genotype. Scale bars are 10 µm. Strains used were DG5020, DG5131, KLG006. See
1161 Table S1 for complete genotypes.
1162
1163
1164 **Figure 3**. The position of the proximal border of the SYGL-1-positive stem cell pool does not
1165 correlate with the position of Sh1. A. Fluorescence confocal maximum projection of surface
1166 images (~7 µm depth) of fixed, dissected gonads showing the SYGL-1-positive stem cell pool
1167 marked in magenta and the sheath cell marked in green. Magenta caret represents the location
1168 of the proximal border of the SYGL-1-positive stem cell pool. Green caret represents the distal
1169 edge of Sh1. B. Quantitative graph with magenta dots representing the proximal border of
1170 SYGL-1::OLLAS expression and green dots representing the distal reach of Sh1. Each pair of dots
1171 connected by a line represents the data for a single gonad. C. Dot plot with overlaid box plots
1172 showing the distance and quantiles of the SYGL-1-positive stem cell pool and distal extent of
1173 Sh1 for each genotype. Each dot represents a single specimen of that genotype. P-values were
1174 calculated using Student's *t*-test. D. Scatterplot showing lack of correlation between the
1175 proximal extent of SYGL-1 expression and the distal reach of Sh1. Scale bars are 10 µm. Strains
1176 used are DG5136, DG5150, DG5181, DG5248, and DG5249. See Table S1 for complete
1177 genotypes.
1178
1179 **Figure 3—figure supplement 1.** The position of the proximal border of the SYGL-1-positive
1180 stem cell pool does not correlate with the position of Sh1 when data are shown in cell

1181 diameters. A. Quantitative graph with magenta dots representing the proximal extent of SYGL-
1182 1::OLLAS expression and green dots representing the distal reach of Sh1. Each pair of magenta
1183 and green dots connected by a line represents the data for a single gonad. B. Dot plot with
1184 overlaid box plots showing the distance and quantiles of the SYGL-1-positive stem cell pool and
1185 distal extent of Sh1 for each genotype, in cell diameters from the distal end. Each dot
1186 represents a single specimen of that genotype. P-values were calculated using Student's *t*-test.
1187 C. Scatterplot showing lack of correlation between the proximal extent of SYGL-1 expression
1188 and the distal reach of Sh1. CD: cell diameters. Strains used are listed in Figure 3.
1189
1190 **Figure 3—figure supplement 2.** Proximal end of the SYGL-1 zone assessed visually and from
1191 protein levels. SYGL-1 (3xOLLAS::SYGL-1) levels were measured from the distal tip of the gonad
1192 to (A) 25 CD and (B) 100 microns proximal, in dissected and stained gonads from 1-day adults
1193 of the indicated genotypes. The visually assessed SYGL-1 border and the distal extent of Sh1
1194 are marked. SYGL-1 protein levels from fluorescence-intensity measurements are normalized
1195 by setting the peak levels in wild type to 100. The SYGL-1 quantitation of the indicated
1196 genotype is carried out for the gonads in Fig. 3B. The small differences observed in SYGL-1 peak
1197 levels between wild type and *inx-14(ag17)* or *inx-8(qy78[mKate2::inx-8])* are not statistically
1198 significant (Student's *t*-test). Triangle, distal most position (start) of Sh1; circle, proximal
1199 position of SYGL-1 staining; blue, wild type; red *inx-14(ag17)*; black *inx-8(qy78[mKate2::inx-8])*.
1200 Curved plot lines, mean; vertical bars, mean ± SD. All three strains have *sygl-1(q983) naIs37 I;*
1201 *bcIs39 V* in the background along with the indicate *inx-x* genotype. Strains used are DG5136,
1202 DG5150, and DG5181. See Table S1 for complete genotypes.
1203
1204
1205 **Figure 4.** The position of the proximal border of the progenitor zone does not correlate with the
1206 position of Sh1. A. Fluorescence confocal maximum projection of surface images (~7 µm depth)
1207 of fixed, dissected gonads showing the progenitor pool marked in magenta and the sheath cell
1208 marked in green. All measurements were made by examining optical sections through the
1209 entire depth of the gonad. Magenta caret represents the location of the proximal border of the

1210 CYE-1-positive, pSUN-1-negative progenitor pool (pSUN-1 staining not shown; see Materials
1211 and Methods). Green caret represents the distal edge of Sh1. B. Quantitative graph with
1212 magenta dots representing the proximal extent of the CYE-1 staining and green dots
1213 representing the distal reach of Sh1. Each pair of magenta and green dots connected by a line
1214 represents the data for a single gonad. C. Dot plot with overlaid box plots showing the distance
1215 and quantiles of the progenitor pool and distal extent of Sh1 for each genotype. Each dot
1216 represents a single specimen of that genotype. P-values were calculated using Student's *t*-test.
1217 D. Scatterplot showing lack of correlation between the proximal PZ border and Sh1 position.
1218 Scale bars are 10 µm. Strains used are DG5136, DG5150, DG5181, DG5248, and DG5249. See
1219 Table S1 for complete genotypes.
1220
1221 **Figure 4–figure supplement 1.** The position of the proximal border of the progenitor zone does
1222 not correlate with the position of Sh1 when data are shown in cell diameters. A. Quantitative
1223 graph with magenta dots representing the location of the proximal border of the CYE-1-
1224 positive, pSUN-1-negative progenitor pool and green dots representing the proximal extent of
1225 and green dots representing the distal reach of Sh1. Each pair of magenta and green dots
1226 connected by a line represents the data for a single gonad. B. Dot plot with overlaid box plots
1227 showing the distance and quantiles of the CYE-1-positive progenitor pool and distal extent of
1228 Sh1 for each genotype, in cell diameters from the distal end. Each dot represents a single
1229 specimen of that genotype. P-values were calculated using Student's *t*-test. C. Scatterplot
1230 showing lack of correlation between the proximal extent of progenitor zone and the distal
1231 reach of Sh1. CD: cell diameters. Strains used are listed in Figure 4.
1232
1233 **Figure 5.** Reduced innexin function shifts Sh1 distally, eliminating the bare regions between the
1234 DTC and Sh1, but this shift does not alter the border of the stem cell pool.
1235

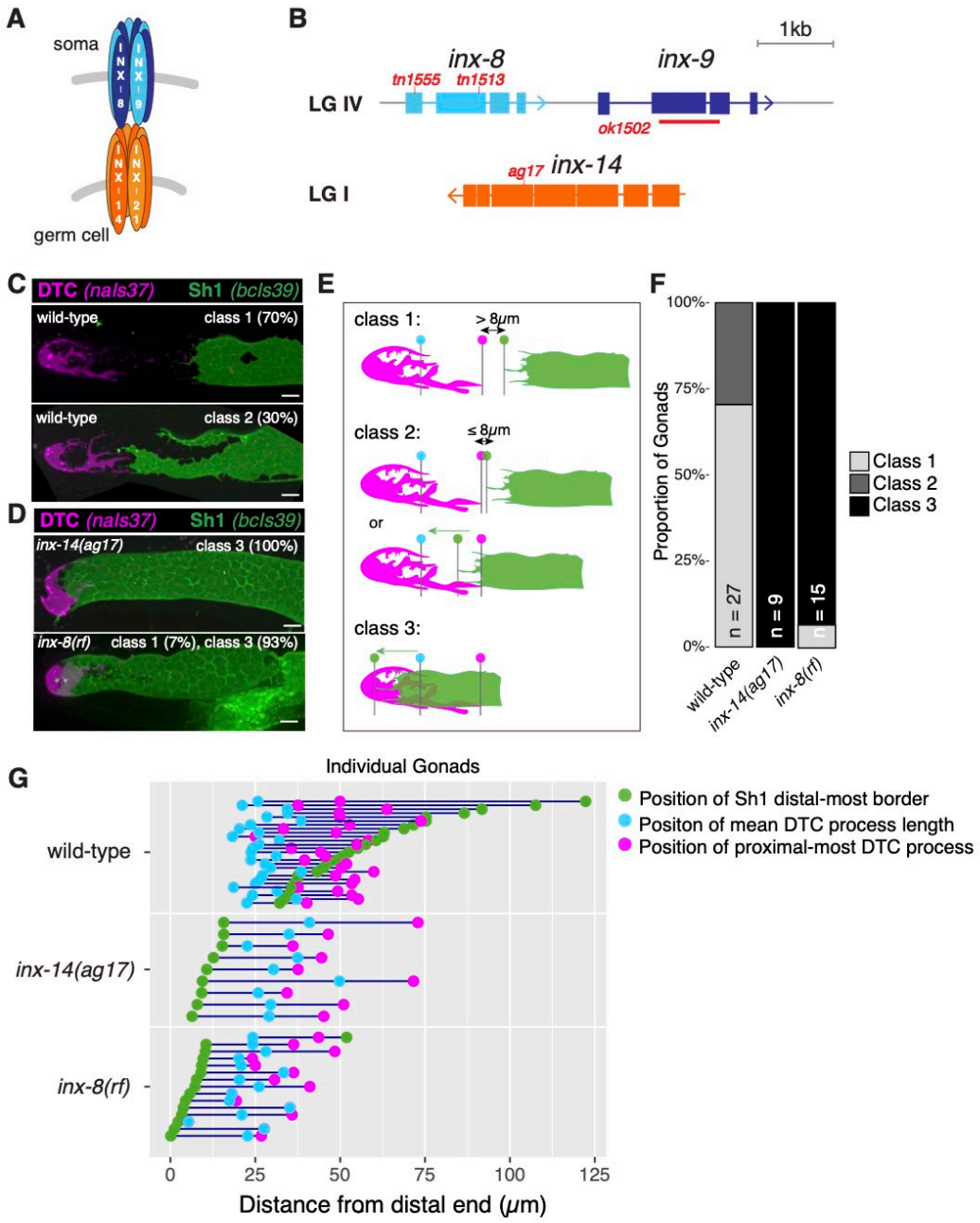

Figure 1

1236

1237

Figure 1—figure supplement 1

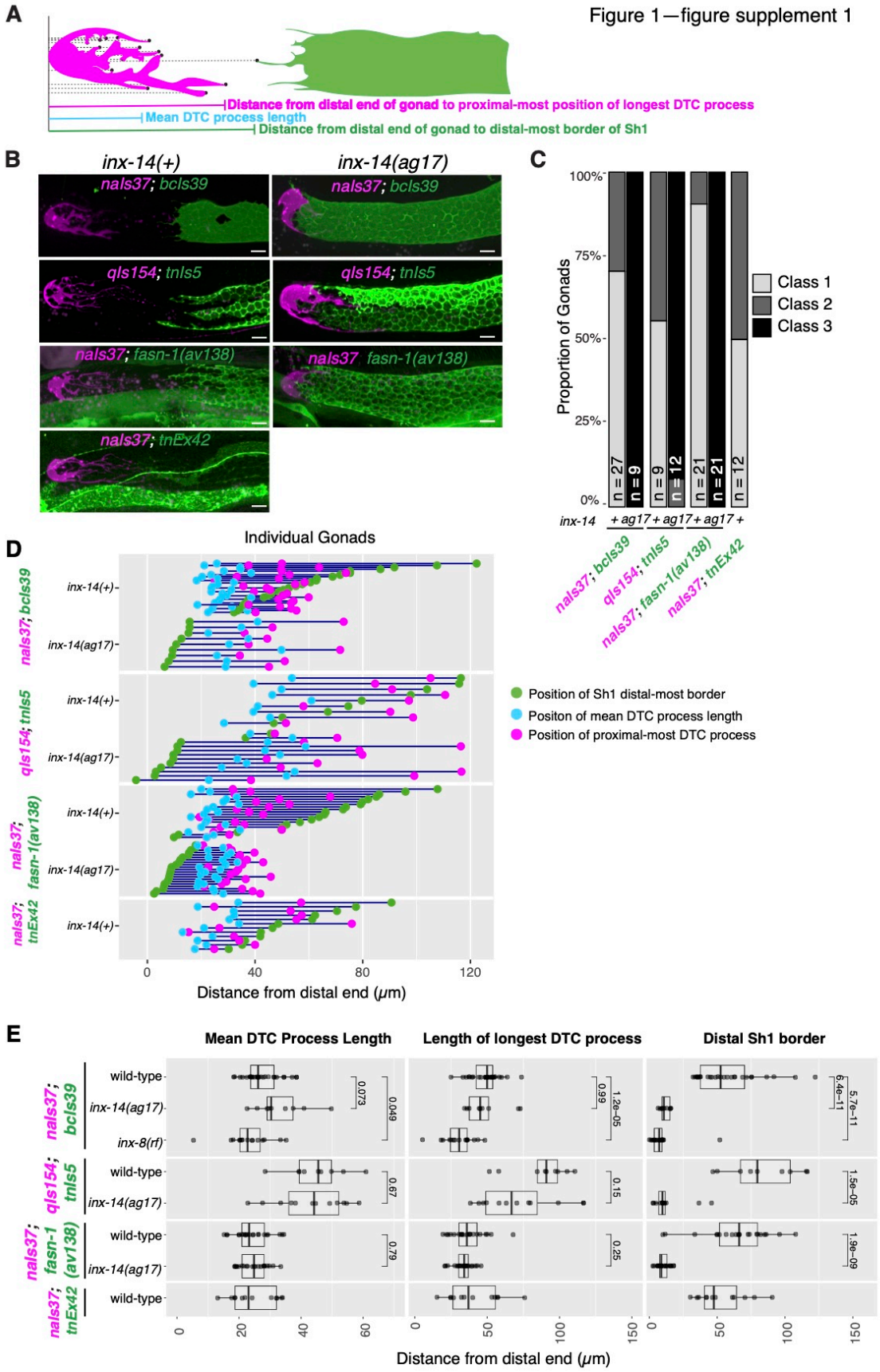

1238

1239

Figure 1—figure supplement 2

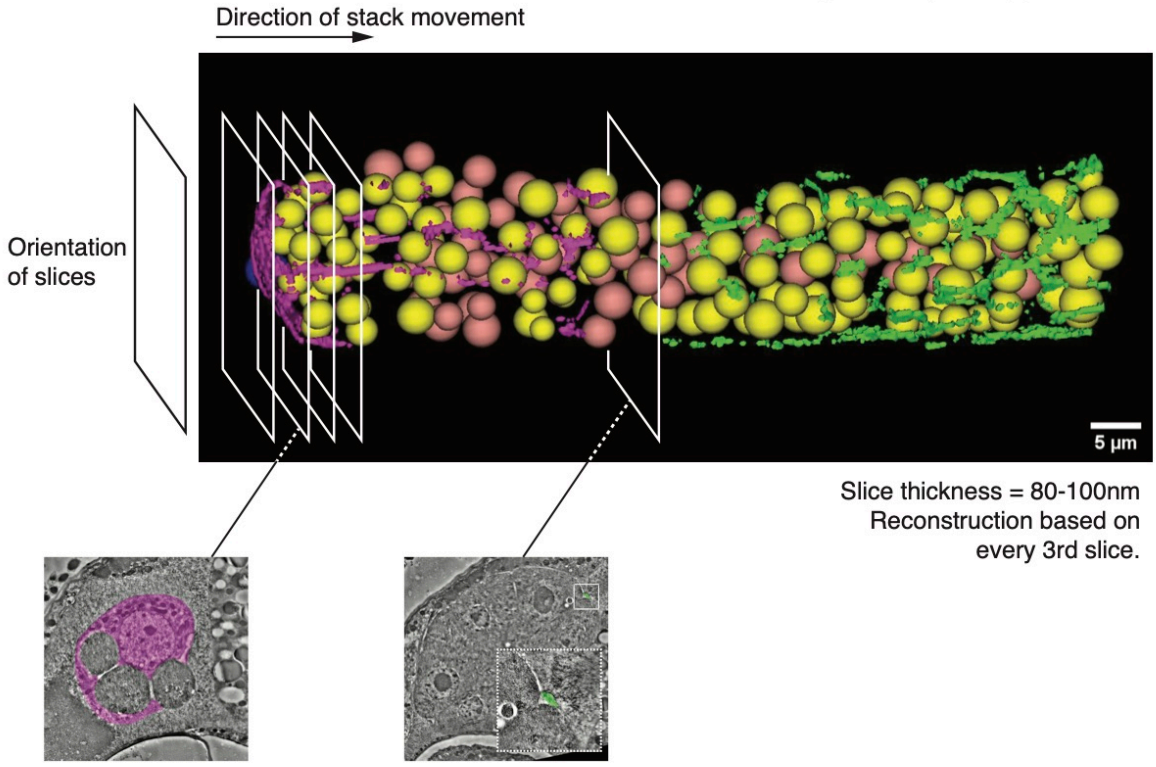

1240

1241

Figure 2

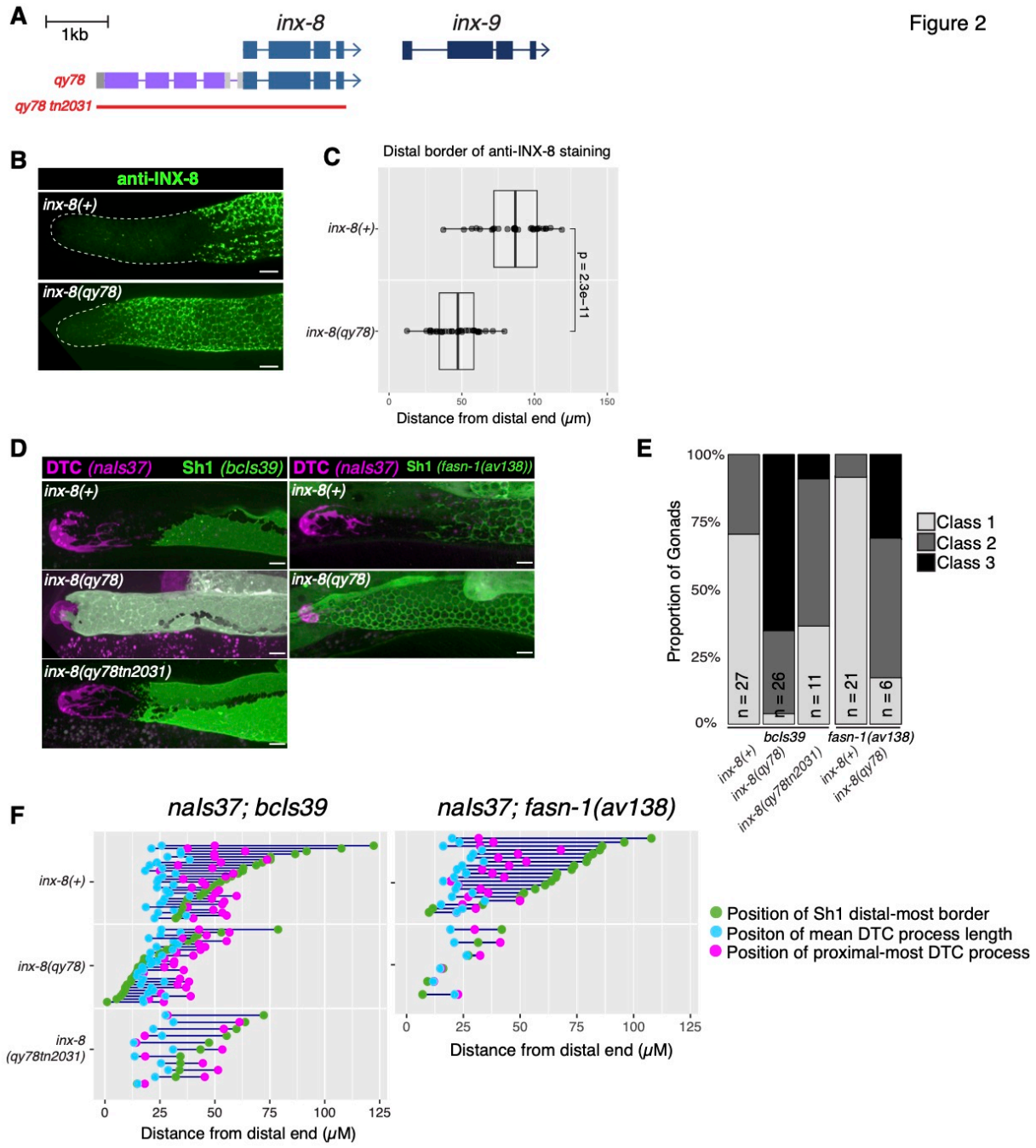
A
1kb
inx-8
inx-9
qy78
qy78 tn2031
B
anti-INX-8
inx-8(+)
inx-8(qy78)
C
Distal border of anti-INX-8 staining
inx-8(+)
inx-8(qy78)
p = 2.3e−11
0
50
100
150
Distance from distal end (μm)
D
DTC (nals37) Sh1 (bcls39)
DTC (nals37) Sh1 (fasn-1(av138))
inx-8(+)
inx-8(qy78)
inx-8(qy78tn2031)
E
100%
75%
50%
25%
0%
Proportion of Gonads
Class 1
Class 2
Class 3
n = 27
n = 26
n = 11
n = 21
n = 6
bcls39
fasn-1(av138)
inx-8(+)
inx-8(qy78)
inx-8(qy78tn2031)
inx-8(+)
inx-8(qy78)
F
nals37; bcls39
nals37; fasn-1(av138)
inx-8(+)
inx-8(qy78)
inx-8 (qy78tn2031)
0
25
50
75
100
125
Distance from distal end (μM)
Position of Sh1 distal-most border
Positon of mean DTC process length
Position of proximal-most DTC process

Figure 2—figure supplement 1

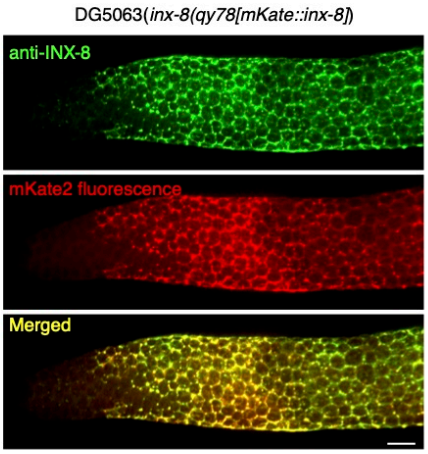

1243

1244

Figure 2—figure supplement 2

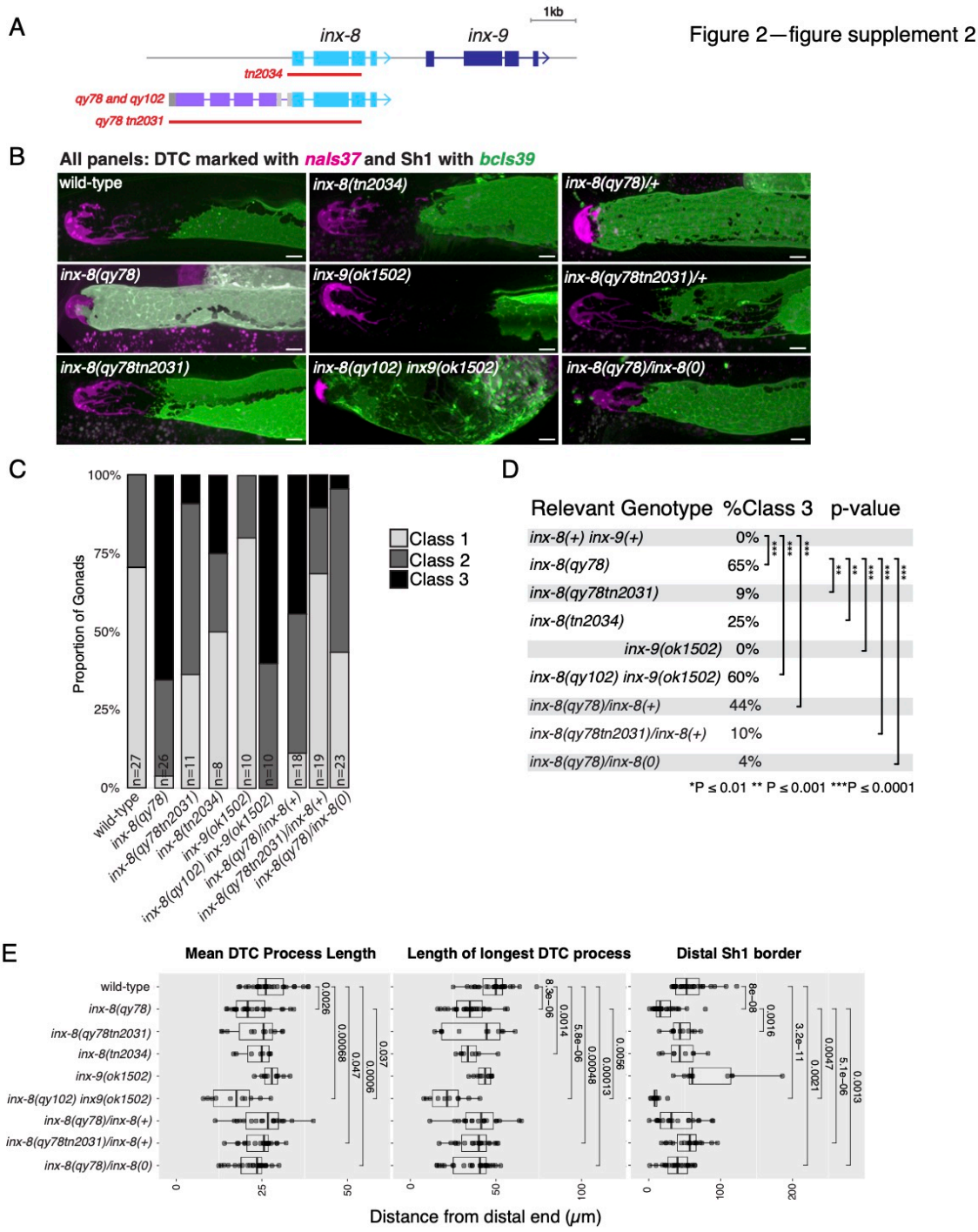

1245
1246

1247

Figure 2—figure supplement 3

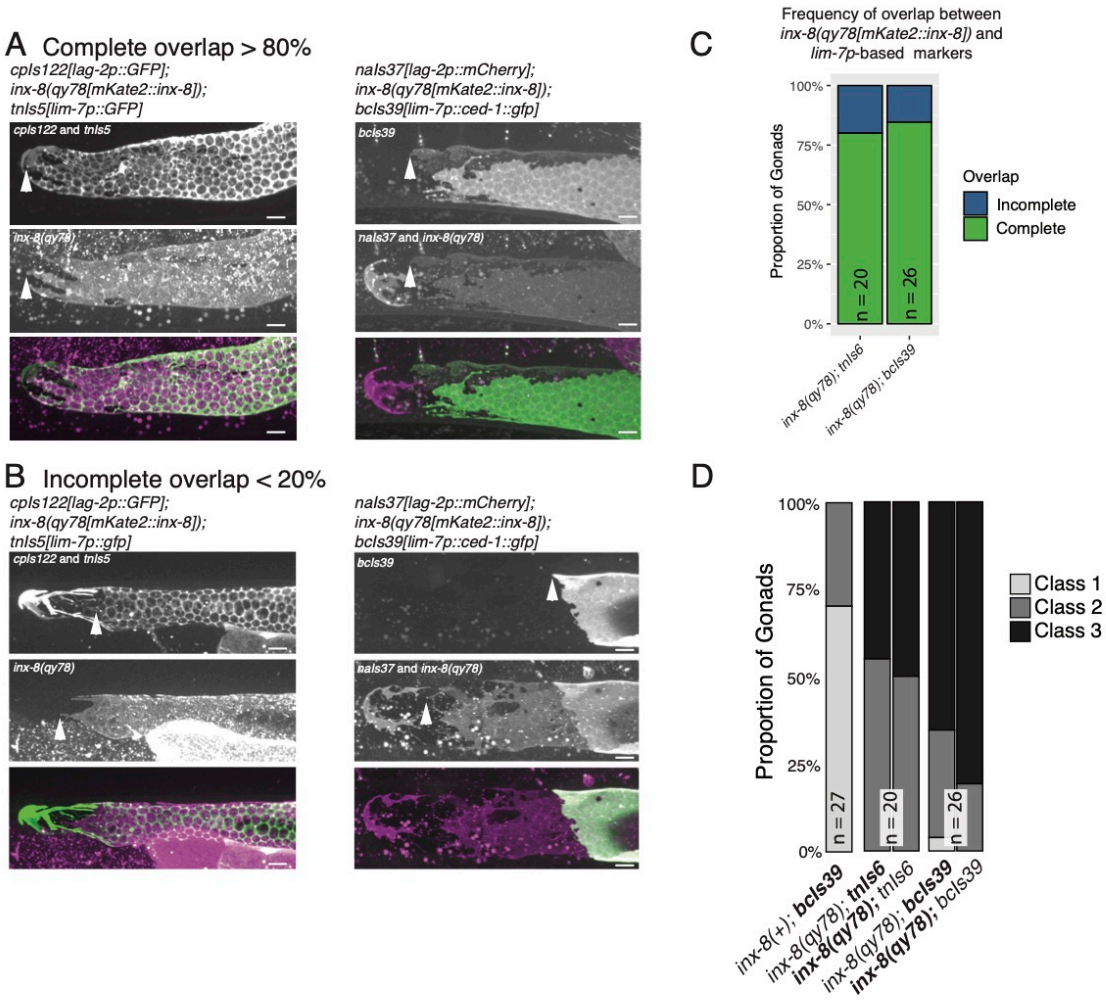

1248

1249

Figure 3

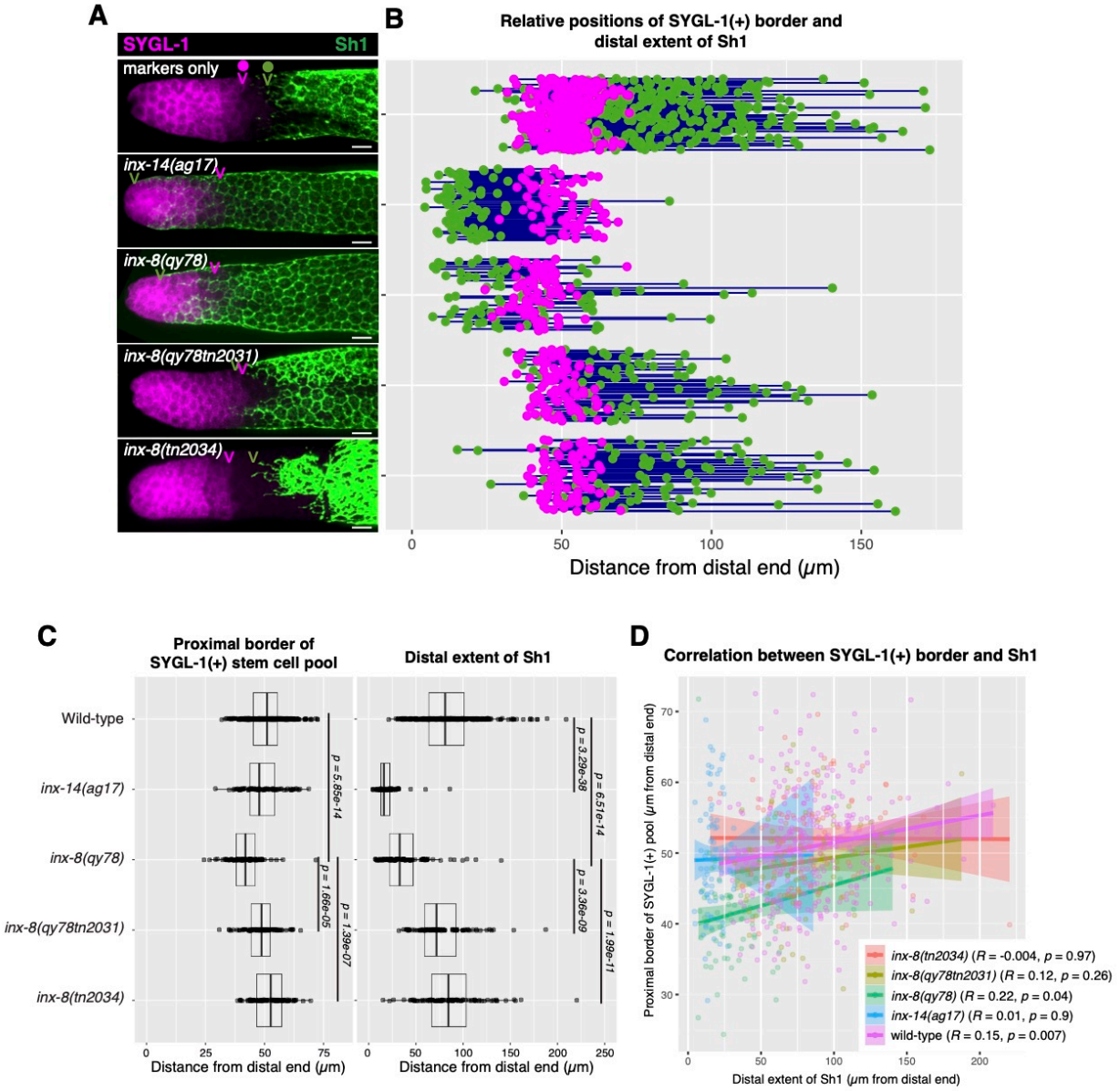

1250

1251

Figure 3—figure supplement 1

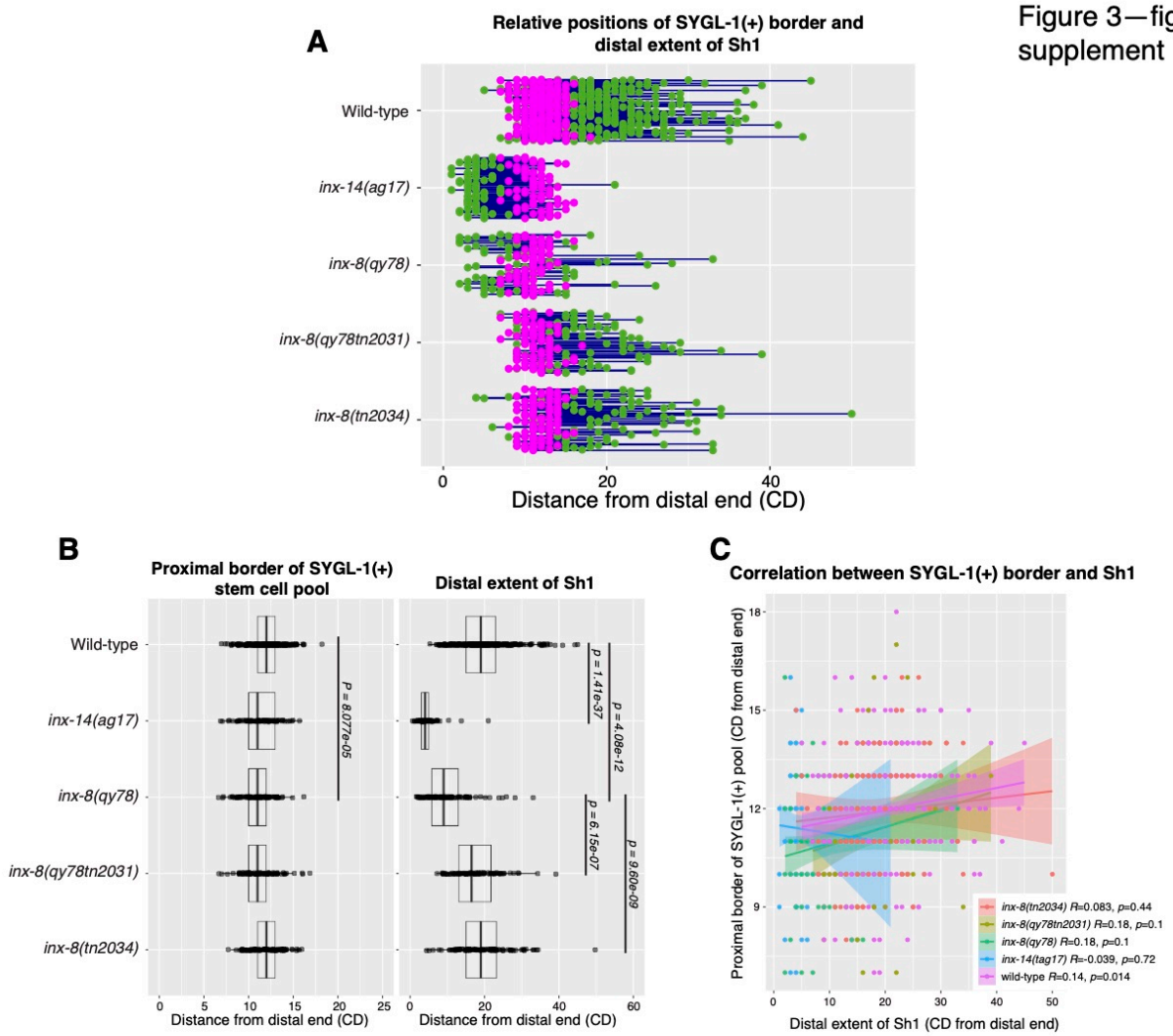

1252

1253

Figure 3—figure supplement 2

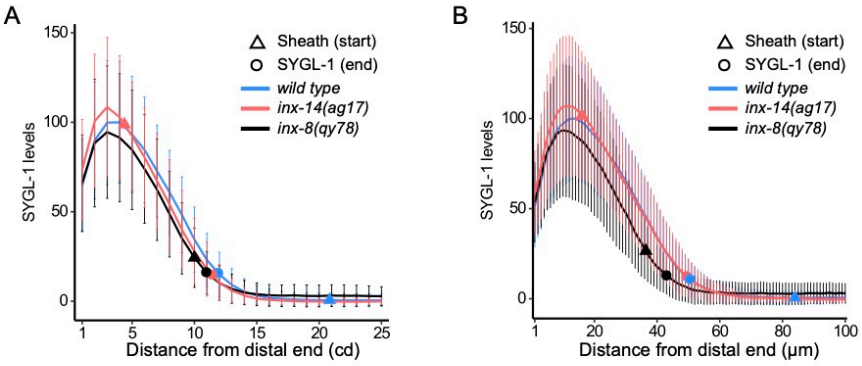

1254

1255

Figure 4

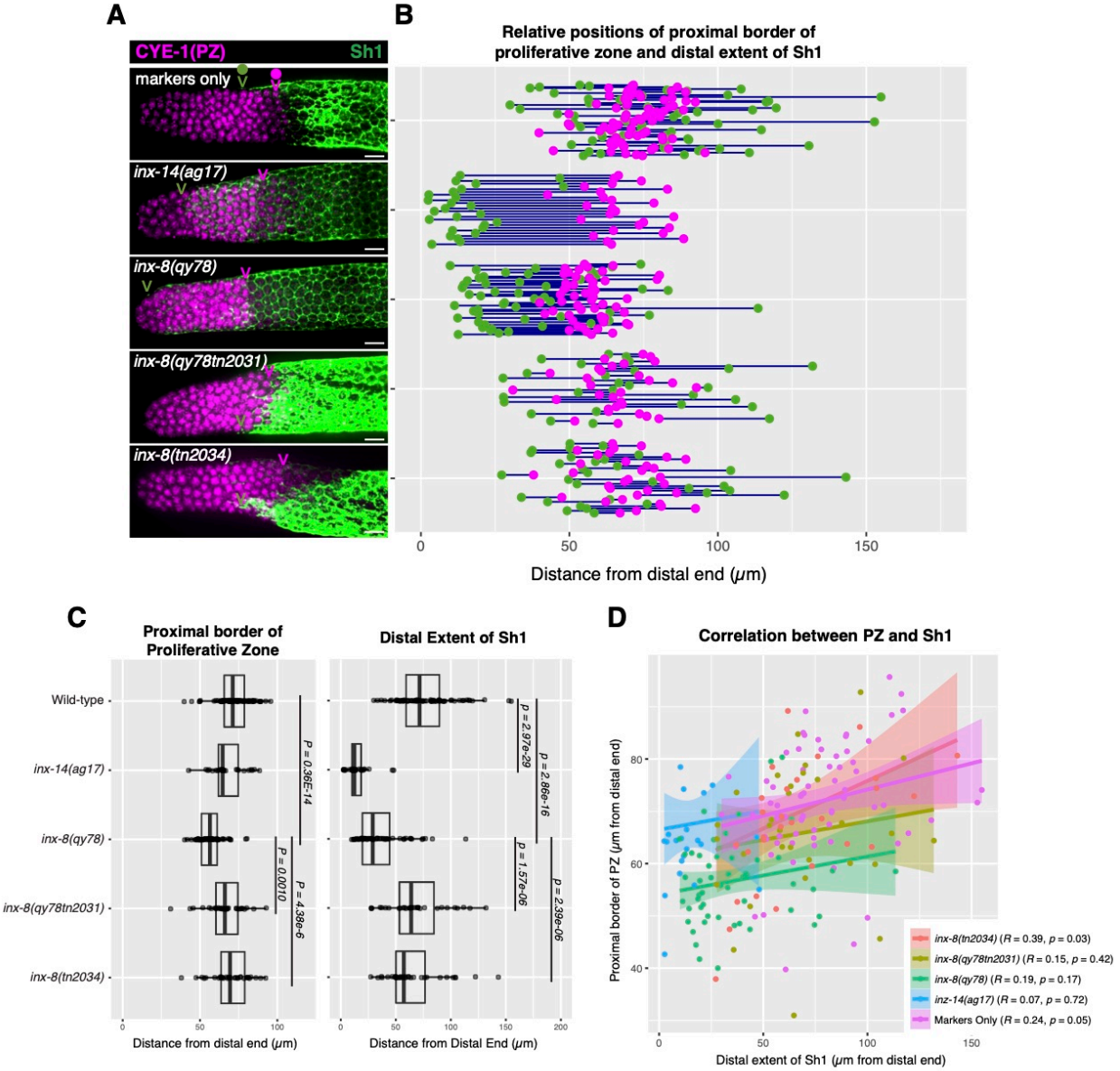

1256

1257

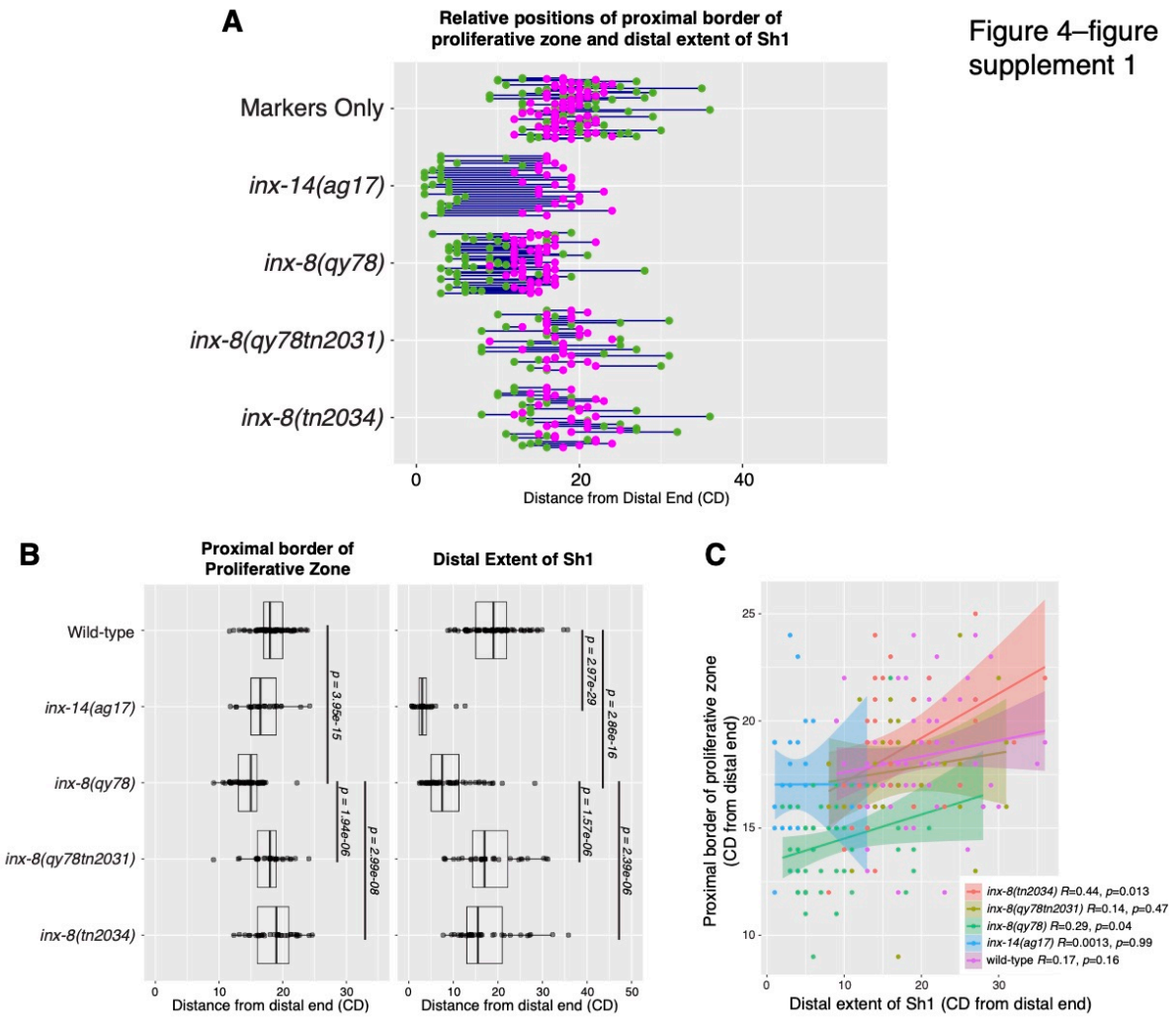

Figure 4–figure supplement 1

1258

1259

Figure 5

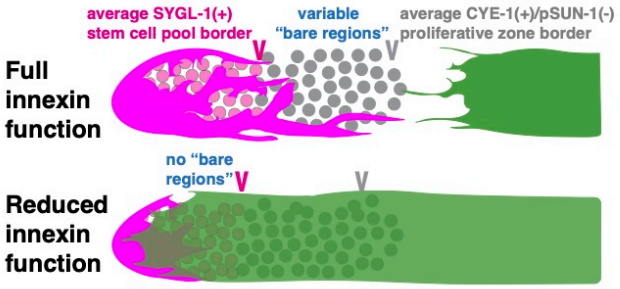

1260